

Self-consistent Stellar Radial Velocities from LAMOST Medium-Resolution Survey (MRS) DR7

BO ZHANG ¹, JIAO LI ², FAN YANG ^{1,3,4}, JIAN-PING XIONG ^{3,4}, JIAN-NING FU ¹, CHAO LIU ², HAO TIAN ²,
YIN-BI LI ³, JIA-XIN WANG ¹, CAI-XIA LIANG ⁵, YU-TAO ZHOU ^{6,7}, WEI-KAI ZONG ¹, CHENG-QUN YANG ⁸,
NIAN LIU ⁹ AND YONG-HUI HOU ^{10,4}

¹*Department of Astronomy, Beijing Normal University, Beijing 100875, People's Republic of China*

²*Key Laboratory of Space Astronomy and Technology, National Astronomical Observatories, Chinese Academy of Sciences, Beijing 100101, People's Republic of China*

³*Key Laboratory of Optical Astronomy, National Astronomical Observatories, Chinese Academy of Sciences, Beijing 100101, People's Republic of China*

⁴*School of Astronomy and Space Science, University of Chinese Academy of Sciences, Beijing, 100049, People's Republic of China*

⁵*National Cancer Center, Peking Union Medical College and Chinese Academy of Medical Sciences, Beijing 100021, People's Republic of China*

⁶*Department of Astronomy, School of Physics, Peking University, Beijing 100871, People's Republic of China*

⁷*Kavli Institute for Astronomy and Astrophysics, Peking University, Beijing 100871, People's Republic of China*

⁸*Shanghai Astronomical Observatory, Chinese Academy of Sciences, Shanghai 200030, People's Republic of China*

⁹*Physics and Space Science College, China West Normal University, Nanchong 637002, People's Republic of China*

¹⁰*Nanjing Institute of Astronomical Optics & Technology, National Astronomical Observatories, Chinese Academy of Sciences, Nanjing 210042, People's Republic of China*

(Received June 1, 2019; Revised January 10, 2019; Accepted May 26, 2021)

Submitted to ApJS

ABSTRACT

Radial velocity (RV) is among the most fundamental physical quantities obtainable from stellar spectra and is rather important in the analysis of time-domain phenomena. The LAMOST Medium-Resolution Survey (MRS) DR7 contains 5 million single-exposure stellar spectra at spectral resolution $R \sim 7500$. However, the temporal variation of the RV zero-points (RVZPs) of the MRS survey, which makes the RVs from multiple epochs inconsistent, has not been addressed. In this paper, we measure the RVs of the 3.8 million single-exposure spectra (for 0.6 million stars) with signal-to-noise ratio (SNR) higher than 5 based on cross-correlation function (CCF) method, and propose a robust method to self-consistently determine the RVZPs exposure-by-exposure for each spectrograph with the help of *Gaia* DR2 RVs. Such RVZPs are estimated for 3.6 million RVs and can reach a mean precision of $\sim 0.38 \text{ km s}^{-1}$. The result of the temporal variation of RVZPs indicates that our algorithm is efficient and necessary before we use the absolute RVs to perform time-domain analysis. Validating the results with APOGEE DR16 shows that our absolute RVs can reach an overall precision of $0.84/0.80 \text{ km s}^{-1}$ in the blue/red arm at $50 < \text{SNR} < 100$, while $1.26/1.99 \text{ km s}^{-1}$ at $5 < \text{SNR} < 10$. The cumulative distribution function (CDF) of the standard deviations of multiple RVs ($N_{\text{obs}} \geq 8$) for 678 standard stars reach $0.45/0.54$, $1.07/1.39$, and $1.45/1.86 \text{ km s}^{-1}$ in the blue/red arm at 50%, 90%, and 95% levels, respectively. The catalogs of the RVs, RVZPs, and selected candidate RV standard stars are available at <https://github.com/hypergravity/paperdata>.

Keywords: methods: data analysis — techniques: radial velocities — (stars:) binaries: spectroscopic

1. INTRODUCTION

Large spectroscopic surveys, for example, RAVE (Steinmetz et al. 2006, 2020a), SDSS/SEGUE (Yanny et al. 2009), LAMOST (Cui et al. 2012; Deng et al. 2012; Zhao et al. 2012; Luo et al. 2015), APOGEE (Majewski

et al. 2017), GALAH (De Silva et al. 2015), *Gaia*-ESO (Gilmore et al. 2012) and *Gaia*-Radial Velocity Spectrometer (*Gaia*-RVS, Katz et al. 2004; Cropper et al. 2018), have obtained tens of millions of stellar spectra over the last two decades, aiming at understanding the formation and evolution of the Galaxy. Among the most fundamental physical quantities derived from stellar spectra is radial velocity (RV) which forms the basis of many studies such as stellar multiplicity (e.g., Gao et al. 2014, 2017; El-Badry et al. 2018; Yang et al. 2020), stellar kinematics (e.g., Tian et al. 2020; Bird et al. 2020), and Galactic substructures (Yang et al. 2019; Xu et al. 2020).

The LAMOST, after a five-year low-resolution spectroscopic survey (LRS, $R \sim 1800$, $3800\text{\AA} < \lambda < 9000\text{\AA}$), has started a five-year medium-resolution spectroscopic survey (MRS, $R \sim 7500$, $4950\text{\AA} < \lambda < 5350\text{\AA}$ and $6300\text{\AA} < \lambda < 6800\text{\AA}$, see Liu et al. 2020) since Sep. 2017. The DR6¹, the first data release of the MRS, contains the data obtained during Sep. 2017 to Jun. 2018 and is already public to the international astronomical community. The DR7² including the data from Sep. 2017 to Jun. 2019 (~ 5 million spectra for over 800 000 stars) is currently open to the Chinese astronomical community only.

At the beginning Sc lamp was used to calibrate the wavelength of LAMOST MRS spectra, and later switched to ThAr lamp in 2018. Due to the short wavelength coverage, sky lines are not used in wavelength calibration as in LRS (Wang et al. 2010). The released spectra have been applied the barycentric correction and the wavelength uses vacuum standard. Both the LAMOST pipeline and Wang et al. (2019) have measured RVs from DR7 spectra and estimated a static RV zero-point (RVZP) by comparing the measured RVs to those in the literature of a sample of RV standard stars (Huang et al. 2018) for each spectrograph. However, the temporal variation of the RVZPs (between exposures) is not clear so far despite a few trials. For example, Liu et al. (2019b) and Zong et al. (2020) show the temporal variation of RVZPs based on the data from the *Kepler* field using a sample of roughly selected RV-invariant stars, and Ren et al. (2020) shows that the RVZPs of the red arm vary between exposures and the difference can reach 4 km s^{-1} in the MRS-N fields (nebula survey, Wu et al. 2020).

Physically, the variation of the LAMOST MRS RVZPs can be explained by several reasons.

1. The LAMOST telescope has a long optical path and a large focal plane (1.75m diameter) on which 4000 fibers are installed Cui et al. (2012), temperature variation is unavoidable.
2. Presently, arc lamp exposures are taken every about 2 hours (typical observing time of a plate) which is not frequent enough. The instrument might change its state between lamp exposures.
3. Since LAMOST MRS needs ~ 20 ThAr lamps to illuminate the big focal plane simultaneously, the decay and replacement of the lamps and the adjustment of lamp exposure time are very often. They affect the signal-to-noise ratio of the lamp spectra and thus the wavelength calibration consistency over time.
4. The MRS spectrographs are mounted and dismounted monthly because the MRS survey is scheduled in the 14 bright/gray nights, while the other nights are for LRS survey. Therefore, the focuses are adjusted monthly.

All these factors and other potential defects in data reduction pipeline are finally reflected in the RVZPs of the spectra. Therefore, it is insufficient to use the RVs either from the LAMOST pipeline or Wang et al. (2019) at different epochs and perform a time-domain analysis, such as in studies of pulsating stars (the LAMOST-*Kepler* project, Zong et al. 2020; Fu et al. 2020), spectroscopic binaries (Gao et al. 2014, 2017; Liu 2019) and even searching for black holes (Liu et al. 2019a; Gu et al. 2019), which are important scientific goals of the MRS survey (Liu et al. 2020).

In this paper, aiming at subsequent time-domain analysis, we measure the RVs for the 3.8 million single-exposure spectra with $\text{SNR} > 5$ in the LAMOST MRS DR7 v1.1³, and propose a robust method to self-consistently determine the absolute RVZPs with the help of the *Gaia* DR2 data. In Section 2, we briefly describe the observational rules of the LAMOST MRS survey and the instrumental parameters. In Section 3, we describe how we measure RVs. In Section 4, we show the algorithm that determines the RVZPs self-consistently. In Section 5, we present our RV and RVZP measurements and assess the precision and self-consistency, and select a sample of candidate RV standard stars based on our results. The information and instruction of our data products are described in Section 6, and the summary of this work is given in Section 7.

¹ <http://dr6.lamost.org/>

² <http://dr7.lamost.org/>

³ <http://dr7.lamost.org/v1.1>

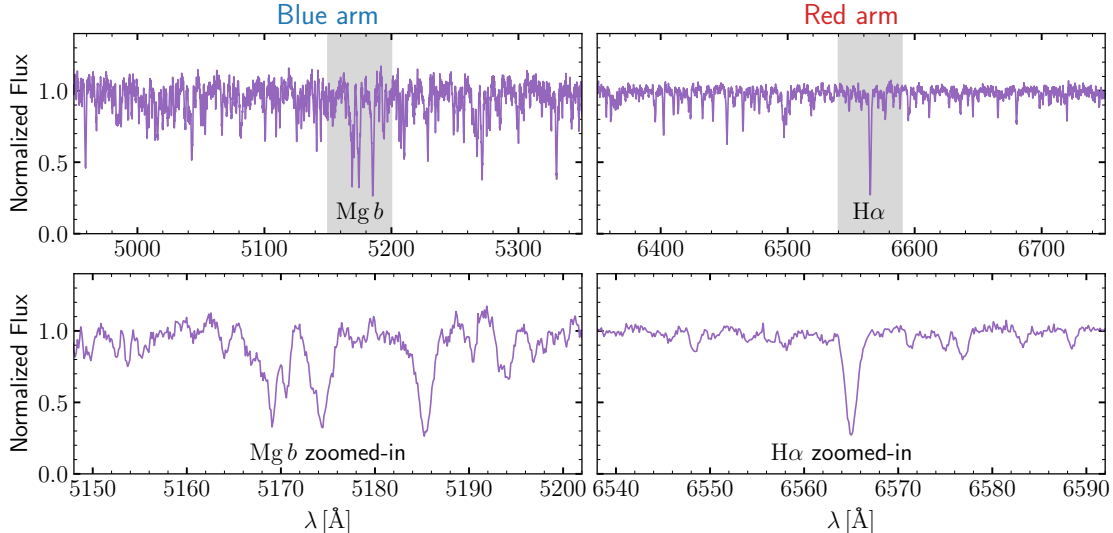


Figure 1. An example of a single-exposure spectrum of a K-type giant star observed in the LAMOST DR7 MRS (med-58649-TD193637N444141K01_sp16-249, RA = 292.719378°, Dec = 46.651537°). The upper panels show the continuum-normalized blue and red arm spectra. The lower panels show the zoomed-in of the upper panels at the Mg *b* and H α region. The zoomed-in regions are shown with gray blocks. The SNRs of the blue and red arm are 29 and 61, respectively.

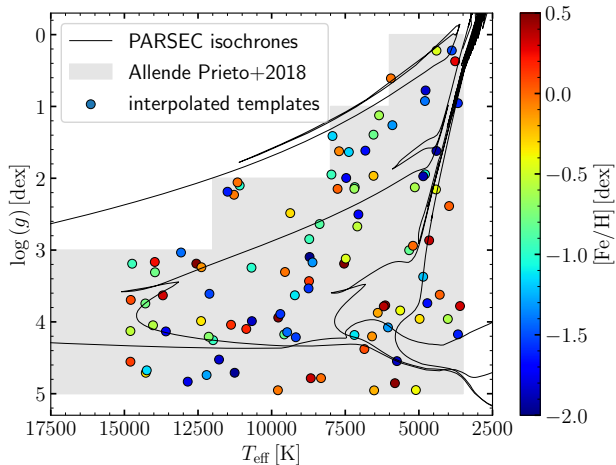


Figure 2. The stellar parameters of the 100 randomly drawn templates that are used in RV measurements. The gray area shows the model grid coverage. The black solid lines are the PARSEC isochrones with solar metallicity and $\log_{10} \tau = 7, 8, 9$ and 10, where τ is age/yr.

2. THE LAMOST MRS SURVEY

2.1. Targeting and Observational Rules

The scientific goals of the LAMOST MRS survey mainly include stellar multiplicity, stellar pulsation, star formation, emission nebulae, Galactic archaeology, host stars of exoplanets, and open clusters. The details of the scientific plan and the survey strategy are described

in (Liu et al. 2020). In this section, we summarize them briefly.

Each scientific goal has a PI who is responsible for its targeting. A **planid** is assigned to each MRS plate (pointing), which has a form of [TD/NT]hhmmss[N/S]ddmmssXnn, where the first two digits denote time-domain (TD, will be repeatedly observed during the five-year survey) or non-time-domain (NT, just observed in a single night), hhmmss[N/S]ddmmss represents for the equatorial coordinate of the plate center and [N/S] means north/south, the digit X is used to denote the scientific goal (see Table 1), and the last two digits represent a serial number. For example, the **planid** TD062610N184524B01 means it is a time-domain plate dedicated to binarity/multiplicity research. There also exists some irregular **planids** which are testing fields, such as HIP8426401, NGC216801, etc. HIP8426401 means the central star of this plate is HIP84264, and NGC216801 means a plate toward the star cluster NGC2168.

The MRS survey uses the Local Modified Julian Minute (LMJM), an 8-bit integer defined as $1440 \times$ the Local Modified Julian Date (LMJD) at the beginning of each exposure, as the stamps of each exposure. Typical exposure time is set to 1200s, while 900s and 600s exposures also exist, depending on the luminosity of targets. Each NT plate is observed with consecutive 3 exposures while each TD plate is observed until it is unobservable (usually 5-6 1200s exposures are allowed). An arc lamp exposure is taken at the beginning of each plate, and at

the end of an observing night (every ~ 2 hours). The targeting is mostly based on *Gaia* DR2 source catalog (Gaia Collaboration et al. 2018). For a 1200s exposure, the magnitudes corresponding to $S/N = 5$ in blue and red arm spectra are $G \sim 14.5$ and 15.2 mag, respectively (see Figure 1 in Liu et al. 2020). Brighter than this magnitude covers the majority of the objects observed by the LAMOST MRS survey.

Table 1. The abbreviation of scientific goals used in `planids`.

X	NT/TD	Science
K	TD	Kepler fields
H	TD	high frequency Kepler fields
B	TD	binarity / multiplicity
T	TD	TESS fields
M	NT	Milky Way
S	NT	star formation
C	NT	star cluster
N	NT	nebula

2.2. The LAMOST MRS Spectra

The whole LAMOST MRS DR7 ($R \sim 7500$) contains over 5 million single-exposure spectra of over 800 000 stars obtained from Sep. 2017 to Jun. 2019. In this work, 3 753 659 spectra with $SNR > 5$ either in blue arm or red arm for 600 771 stars are selected. Their distributions on number of exposures and time span is presented in Figure 3. The spectra are oversampled. Typical wavelength steps are 0.11 and 0.14 \AA at the blue and red arm, respectively. The sampling rate ($\lambda/\Delta\lambda \sim 45\,000$) is as high as 6 times the spectral resolution ($R \sim 7500$). In Figure 1, we show a spectrum of a K-type giant star as a demo of the LAMOST MRS survey. The blue arm and red arm are designed mainly for the Mg I b triplet at around 5 175 \AA and H α at around 6 564 \AA . The released spectra are not corrected with response curves.

3. MEASURE RADIAL VELOCITIES

3.1. Preparation for RV Measurements

We noticed that cosmic rays frequently pollute the MRS single-exposure spectra and are neither identified nor removed by the LAMOST pipeline. Therefore, in our method, the first step is to carefully remove the cosmic rays in spectra. We smooth spectra with a 21-pixel median filter followed by a 9-pixel Gaussian filter, and remove the original pixels which deviate from the smoothed spectrum by 4 and 8 times the local standard deviation in the upper and lower direction. The

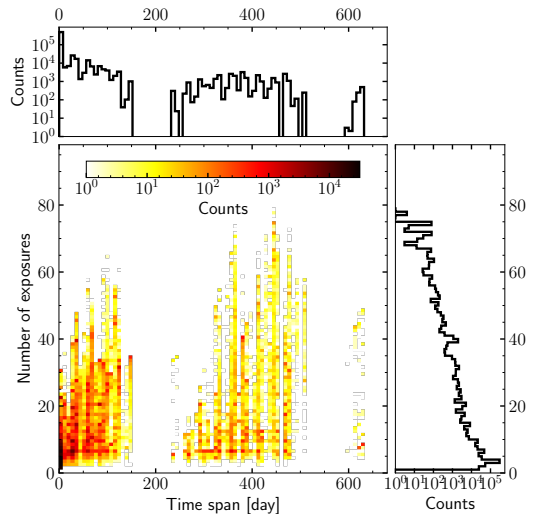


Figure 3. The distributions of the number of exposures and the time span of the stars observed in LAMOST MRS DR7.

parameters of the filters are set empirically so that the absorption lines in the spectra of A-, F-, G- and K-type stars are not affected. The removed pixels are replaced by values linearly interpolated using neighboring pixels. We also note that the two ends of both blue and red arms are sometimes tilted and show unreasonable flux values probably due to extrapolation of the sky flux modeling, so we trim the 50 pixels at both edges of each arm.

The second step is to normalize spectra to pseudo-continuum to place the spectral features (usually absorption lines) on the same scale. We iteratively fit the spectrum with a smoothing spline function and clip the pixels away from the median values by 3 times the standard deviation in each 100 \AA window. The number of iterations is set to 3. As shown in Figure 1, for a typical K-type star with medium SNR, the normalization is quite adequate for the subsequent RV measurements.

3.2. Spectral Templates

We adopt the synthetic grid published by Allende Prieto et al. (2018) based on the ATLAS9 stellar atmosphere model (Kurucz 1979; Mészáros et al. 2012) as our spectral library. We degrade the spectral resolution from 10 000 to 7 500 to fit the MRS configuration and converted from air wavelength to vacuum wavelength using the formula proposed by Morton (2000). To limit the computational cost of the subsequent RV measurements at a reasonable amount, we interpolate the synthetic library to generate 100 spectral templates with stellar parameters randomly drawn from a uniform distribution in the range $3500 < T_{\text{eff}}/\text{K} < 15000$, $0 < \log g/\text{dex} < 5$, $-2 < [\text{Fe}/\text{H}]/\text{dex} < 0.5$ and $-0.5 < [\alpha/\text{Fe}]/\text{dex} < 0.7$. Extremely metal-poor and extremely hot templates are

not considered because the spectral features are not significant. Tests on high-SNR MRS spectra show that the sparsity of our templates induces a statistical error ~ 0.10 and 0.20 km s^{-1} in the blue and red arm, respectively, which are negligible compared to other sources of uncertainties. Figure 2 shows the distribution of parameters of the 100 spectral templates and a series of PARSEC isochrones (Bressan et al. 2012) with solar metallicity and logarithmic age $\log_{10} \tau = 7, 8, 9$ and 10 . These spectral templates are normalized to pseudo-continuum using the same way as in Section 3.1.

3.3. RV Estimates

The cross-correlation function (CCF, Tonry & Davis 1979) method is widely used in spectroscopic surveys to measure stellar RVs (e.g., Nidever et al. 2015; Steinmetz et al. 2020b). One important advantage is that the CCF can be accelerated using Fast Fourier Transformation (FFT) once the spectrum is continuum-subtracted and re-sampled to a logarithmic wavelength grid. However, the drawback of such a scheme is that the sampling of the resulting CCF is generally very sparse. To evaluate the CCF at a smaller RV step, we do not follow the FFT way. In our implementation, the CCF at an RV of v is evaluated as

$$\text{CCF}(v|\mathbf{F}, \mathbf{G}) = \frac{\text{Cov}(\mathbf{F}, \mathbf{G}(v))}{\sqrt{\text{Var}(\mathbf{F})\text{Var}(\mathbf{G}(v))}}, \quad (1)$$

where \mathbf{F} is the vector of the normalized observed spectrum, $\mathbf{G}(v)$ is the vector of normalized synthetic spectrum shifted by an RV (v) and resampled to the wavelength grid of \mathbf{F} , Var represents the variance operator, and Cov represents the covariance operator (see Appendix A for more details).

Deriving the final RV consists of three steps.

1. The initial estimates are made from an RV grid from -1500 to 1500 km s^{-1} , with a step of 10 km s^{-1} . The template with the maximum CCF value is selected as the best-match template, and the corresponding radial velocity is adopted as the initial guess of the final RV of the observed star. And the parameters of the template (T_{eff} , $\log g$, $[\text{Fe}/\text{H}]$, $[\alpha/\text{Fe}]$) are recorded, which make a good prior for some following analysis such as stellar atmospheric parameter determination.
2. With the best-match template, we maximize the CCF to determine the final RV (v_{obs}) using the optimization routine `scipy.optimize.minimize` with the Nelder-Mead algorithm (Nelder & Mead 1965). The corresponding CCF value is recorded as CCFMAX to assess the likelihood between the

best-match template and the observed spectrum. The SNR–CCFMAX relations are shown in Figure 4.

3. To obtain the measurement error $\sigma_{v,\text{obs}}$, we use a Monte Carlo method, namely, we repeat this process 100 times and in each time we add Gaussian random noise to the spectrum according to the flux error. The measurement error is computed using 16th and 84th percentiles, i.e., $\sigma_{v,\text{obs}} = (v_{84} - v_{16})/2$. The SNR– $\sigma_{v,\text{obs}}$ relations are shown in Figure 5.

We avoid the Gaussian fitting to the CCF which is widely used in literature (e.g., Nidever et al. 2015; Wang et al. 2019). The reasons for doing this include that the CCF peak is obviously non-Gaussian and that at low signal-to-noise ratio (SNR) the fitting process is fragile. The final error of RV includes measurement error and a noise floor term which is due to (**Replaced: systematics** replaced with: **systematics**) (e.g., background, detector imperfections, temperature changes, focusing issues, etc) and will be assessed in the following part of this paper.

In this work, one RV is estimated for the blue arm (v_{B}) and two for the red arm (v_{R} and v_{Rm}). The v_{Rm} is measured using the H α -masked red arm spectrum. As shown in Figure 4 and 5, these RV measurements deteriorate rapidly at $\text{SNR} < 20$. For cool stars (e.g., FGK type), at a given SNR, v_{B} is more precise than v_{R} because of rich spectral features in blue arm (for a detailed discussion of spectral information content in MRS spectra, see Zhang et al. 2020b). However, for hot stars, v_{R} is more reliable because of the H α feature and v_{Rm} is significantly less precise than v_{R} H α . Therefore, we recommend the readers to only consider v_{Rm} when the targets have H α emission.

4. RADIAL VELOCITY ZERO-POINTS

In essence, the RV zero-point (RVZP) is the bias of the wavelength solution of a specific spectrum compared to its *true* wavelength solution in terms of radial velocity. It is affected by many factors, e.g., the condition of the instrument, the quality of the arc lamp exposure, the reduction algorithm, and the non-simultaneous nature of the arc lamp exposure and the object exposure, etc. In this paper, we define the RVZP correction value Δv by

$$v_{\text{abs}} = v_{\text{obs}} + \Delta v, \quad (2)$$

where v_{abs} is the absolute radial velocity and v_{obs} the radial velocity directly measured from a spectrum.

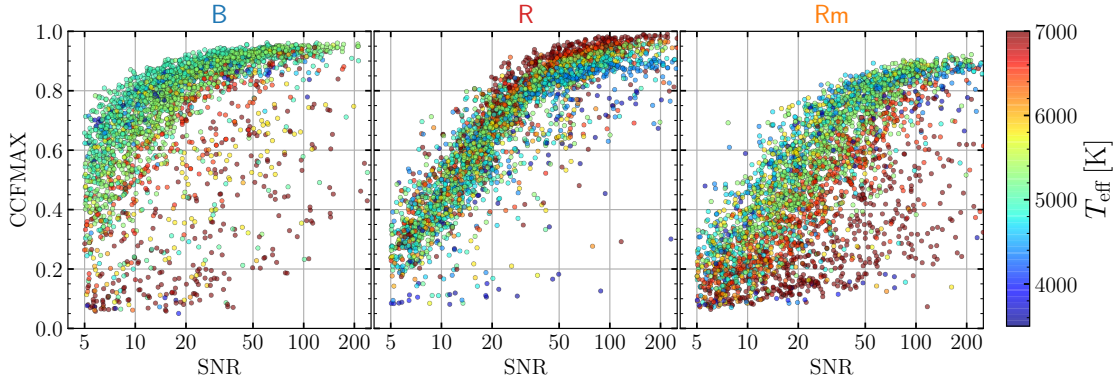


Figure 4. The left/middle/right panel shows the SNR–CCFMAX relation for B(blue arm)/R(red arm)/Rm(red arm with H α masked) CCF results of 5000 randomly selected spectra, respectively. Color denotes the T_{eff} of the best-match template.

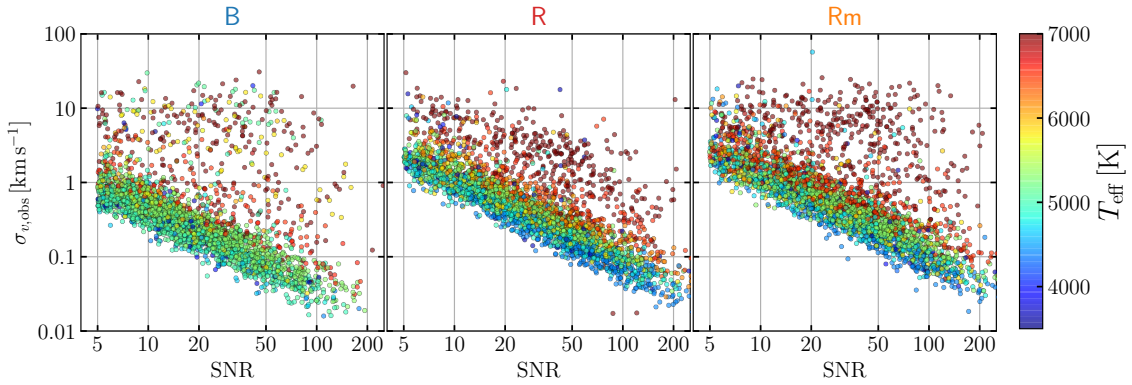


Figure 5. The left/middle/right panel shows the SNR– $\sigma_{v,\text{obs}}$ (measurement error) relation for B(blue arm)/R(red arm)/Rm(red arm with H α masked) CCF results of 5000 randomly selected spectra, respectively. Color denotes the T_{eff} of the best-match template.

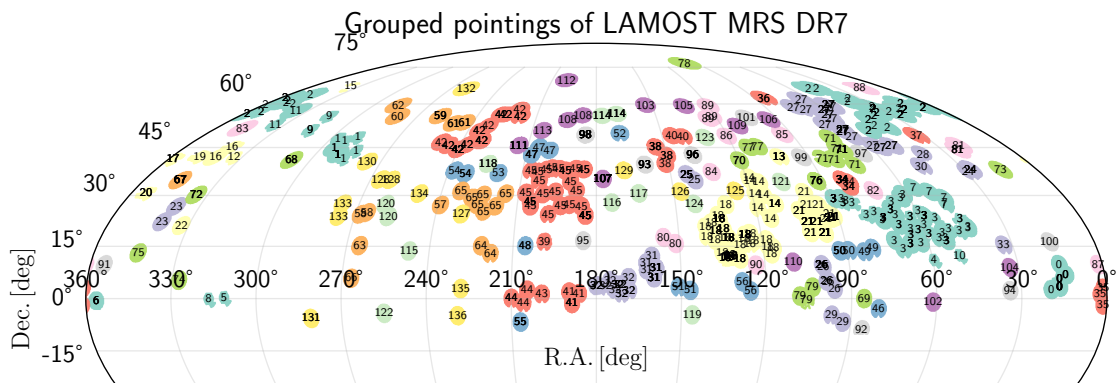


Figure 6. Grouped pointings of the LAMOST DR7 MRS observations using a friends-of-friends method with a linking length of 5 degrees. The field-of-view of LAMOST is a circle with 2.5-degree radius if all spectrographs are at work. The figure uses equatorial coordinate system with Mollweide projection, and the pointings in a particular group are shown with the same color.

4.1. The Scheme

The LAMOST has 16 spectrographs of which each has 250 fibers (4000 fibers in total). Excluding a few tens

of sky fibers and a few problematic fibers, each spectrograph typically produces $\lesssim 200$ spectra in an exposure, depending on targeting, the condition of the instrument, the data quality, and the reduction algorithm. Let i de-

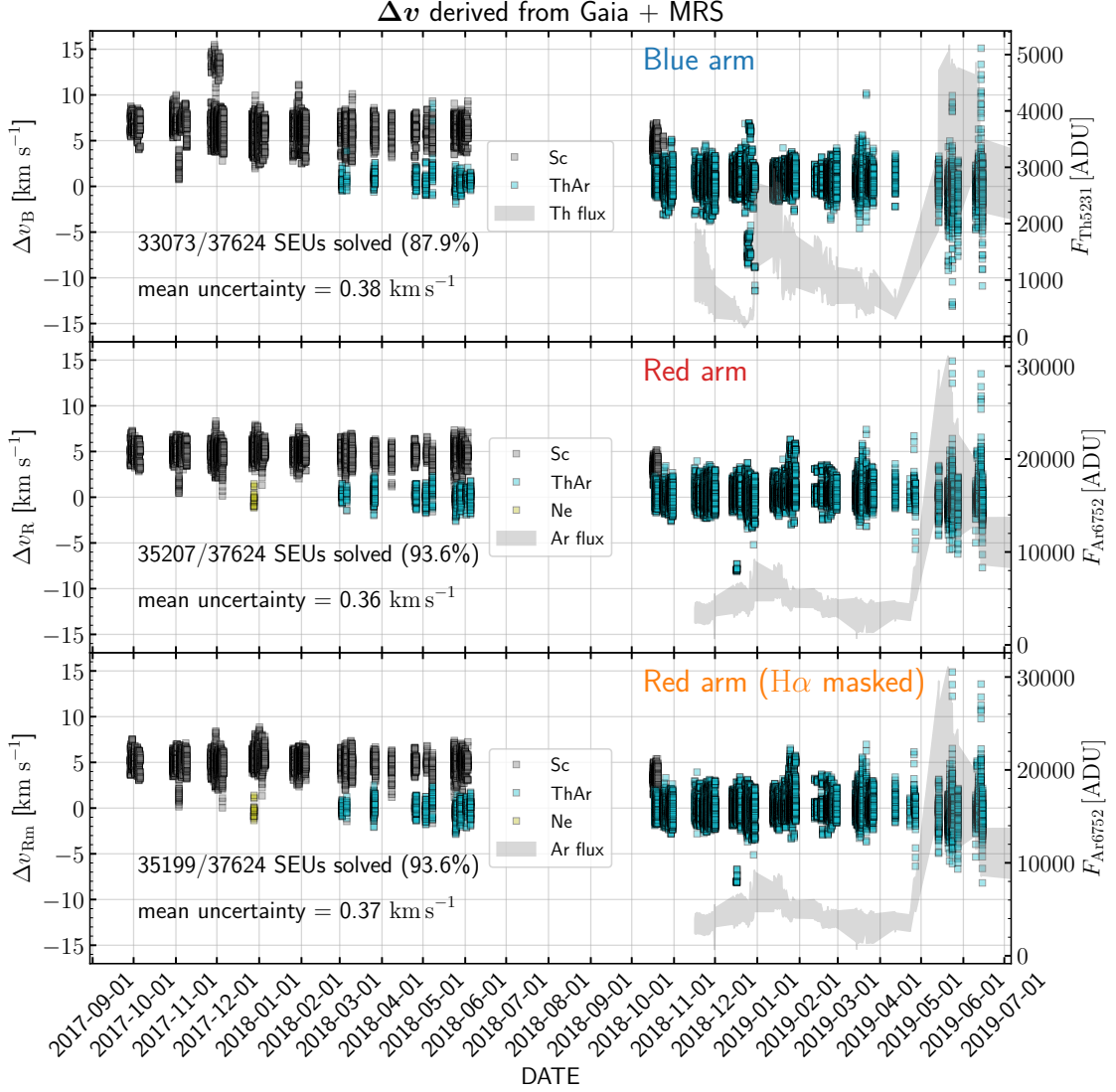


Figure 7. The temporal variations of the RVZP correction values for the blue arm (Δv_B), red arm (Δv_R), and $H\alpha$ -masked red arm (Δv_{Rm}), are shown in the top, middle and bottom panels, respectively. The gray/cyan/olive square markers show the RVZP correction values of SEUs calibrated with Sc/ThAr/Ne lamp in LAMOST MRS DR7. The max/min peak flux of Th 5231 Å and Ar 6752 Å of the 16 spectrographs are shown using gray area.

note the exposure epoch or LMJM, j the spectrograph ID, and k the fiber ID, ideally, we seek for the solution of the RVZP for each fiber, each spectrograph, and exposure by exposure, namely, the $\Delta v_{i,j,k}$. This scheme is infeasible because the true/reference RVs $v_{i,j,k,abs}$ of the targets are not always known.

In this work, assuming that the fibers in a spectrograph in one exposure (hereafter, we refer to it as a spectrograph-exposure-unit, or an SEU) share similar RVZPs, the systematic RVZP $\Delta v_{i,j}$ can be determined as long as a homogeneous reference set of RVs can be found for a fraction of fibers in that SEU. The assumption is quite reasonable given the fact that the wave-

length calibration of a multi-fiber spectrograph is done by fitting a 2D grating equation. And, as we will see in Section 4.2, the Gaia DR2 RVs (Katz et al. 2019) meet our needs for the reference set.

As a contrast, both the LAMOST pipeline and Wang et al. (2019) calculate Δv_j assuming the RVZPs for a specific spectrograph do not vary with time, and, therefore, get around the temporal variation of RVZPs. However, we noticed that there exist some weird absolute RVs (as we will see in the results in Section 5).

4.2. The Gaia DR2 RVs as the Reference Set

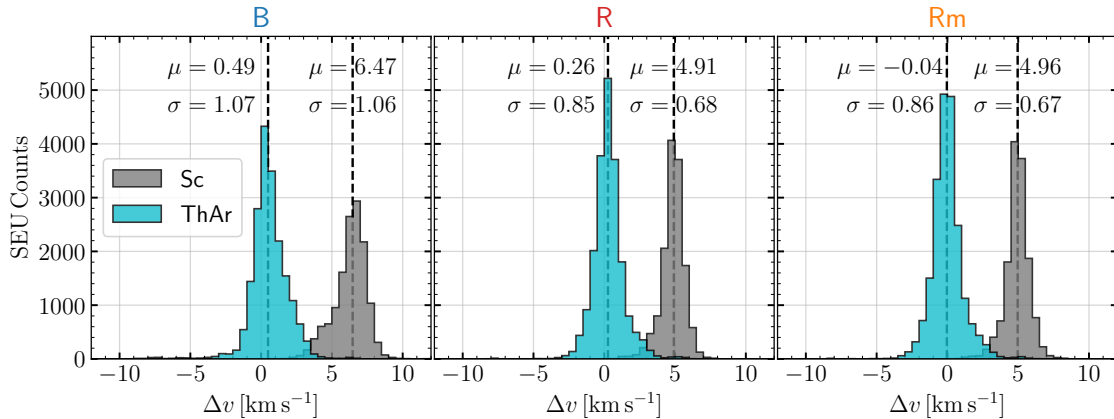


Figure 8. The histograms of the Δv_B , Δv_R and Δv_{Rm} . Sc and ThAr lamp-calibrated data are shown in gray and cyan, respectively. The μ s and σ s are calculated using the median and $(q84 - q16)/2$, respectively.

Thanks to the ESA *Gaia* mission (Gaia Collaboration et al. 2016), providing us the largest RV dataset that matches the LAMOST MRS survey in velocity precision and magnitude limit. The spectral resolution of *Gaia*-RVS ($R \sim 11\,500$, Cropper et al. 2018) is slightly higher than the MRS ($R \sim 7\,500$). The magnitude limit of the *Gaia* DR2 RV catalog (Katz et al. 2019) is at $G_{RVS} = 12$ mag or $G \sim 14$ mag depending on spectral type and line-of-sight interstellar extinction, which is slightly brighter than the LAMOST MRS magnitude limit. The *Gaia* DR2 contains qualified median radial velocities for 7 224 631 stars derived from the *Gaia*-RVS spectra, with T_{eff} in the range [3550, 6900] K excluding large RV variant stars (see Katz et al. 2019, for details). At the faint end, $G_{RVS} = 11.75$ mag, the precisions for $T_{\text{eff}} = 5000$ and 6500 K are 1.4 and 3.7 km s^{-1} , respectively.

Aiming at studying time-domain astrophysical phenomena, e.g. spectroscopic binaries, we proceed to carry out the second-best scheme – $\Delta v_{i,j}$. Cross-matching the LAMOST MRS DR7 catalog with the *Gaia* DR2, 1 582 948 out of 3 753 659 single-exposure spectra (42.1%) have *Gaia* RVs, and the common objects usually have good SNR in MRS because they are relatively bright in LAMOST MRS. The number of objects in *Gaia* DR2 is $\sim 1\,000$ times larger than that in catalogs of RV standard stars such as Huang et al. (2018). The challenge arises because not all of the 7 million objects in the *Gaia*-RVS catalog are RV invariant, i.e., quite a number of them are pulsating stars or binary/multiple systems that have periodic/non-periodic RV variations. In the below, we demonstrate a robust method that can determine the RVZP self-consistently for each spectrograph in each exposure ($\Delta v_{i,j}$) by com-

paring the observed RVs to the *Gaia* DR2 RVs without identifying RV standard stars.

4.3. Self-consistent RVZPs

Assuming that the RV variables are varying with random periods at random phases or non-periodically, and are not the majority of the observed stars, we can regard them as outliers and use a robust method, e.g. the Least Absolute Residual (LAR) regression (or Least Absolute Deviation regression, see Press et al. 2002), to estimate the $\Delta v_{i,j}$ (the common RV bias shared by the objects in an SEU). From a Bayesian perspective, the LAR regression originates from an exponential likelihood while Least Squares (LSQ) regression comes from a Gaussian likelihood. Utilizing the LAR technique, extreme values have a lesser influence on the fit compared to the LSQ regression. Besides, since we aim at time-domain analysis, as long as our RVZPs are temporally self-consistent, the absolute scales are not very important.

Using the indices proposed in Section 4.1, for each group of pointings, we construct a global cost function f as below,

$$f(\Delta \mathbf{v}) = \Lambda_1 \sum_i \sum_j \sum_k \frac{|v_{i,j,k,\text{obs}} + \Delta v_{i,j} - v_{i,j,k,\text{GAIA}}|}{\sqrt{\sigma_{\text{min}}^2 + \sigma_{i,j,k,\text{obs}}^2 + \sigma_{i,j,k,\text{GAIA}}^2}} + \Lambda_2 \sum_i \sum_j \sum_k \frac{|v_{i,j,k,\text{obs}} + \Delta v_{i,j} - \bar{v}_{i,\text{obs}}|}{\sqrt{\sigma_{\text{min}}^2 + \sigma_{i,j,k,\text{obs}}^2 + \sigma_{i,j,\text{obs}}^2}}, \quad (3)$$

where $\Delta \mathbf{v}$ is the vector of $\{\Delta v_{i,j}\}$ for all relevant SEUs in the group of pointings, $v_{i,j,k,\text{obs}}$ and $\sigma_{i,j,k,\text{obs}}$ are the RV and associated measurement error of the k th star in the SEU $\{i, j\}$, $v_{i,j,k,\text{GAIA}}$ and $\sigma_{i,j,k,\text{GAIA}}$ are the *Gaia* RV and associated uncertainty of the k th star in SEU $\{i, j\}$, σ_{min} is the noise floor of the measured RV which

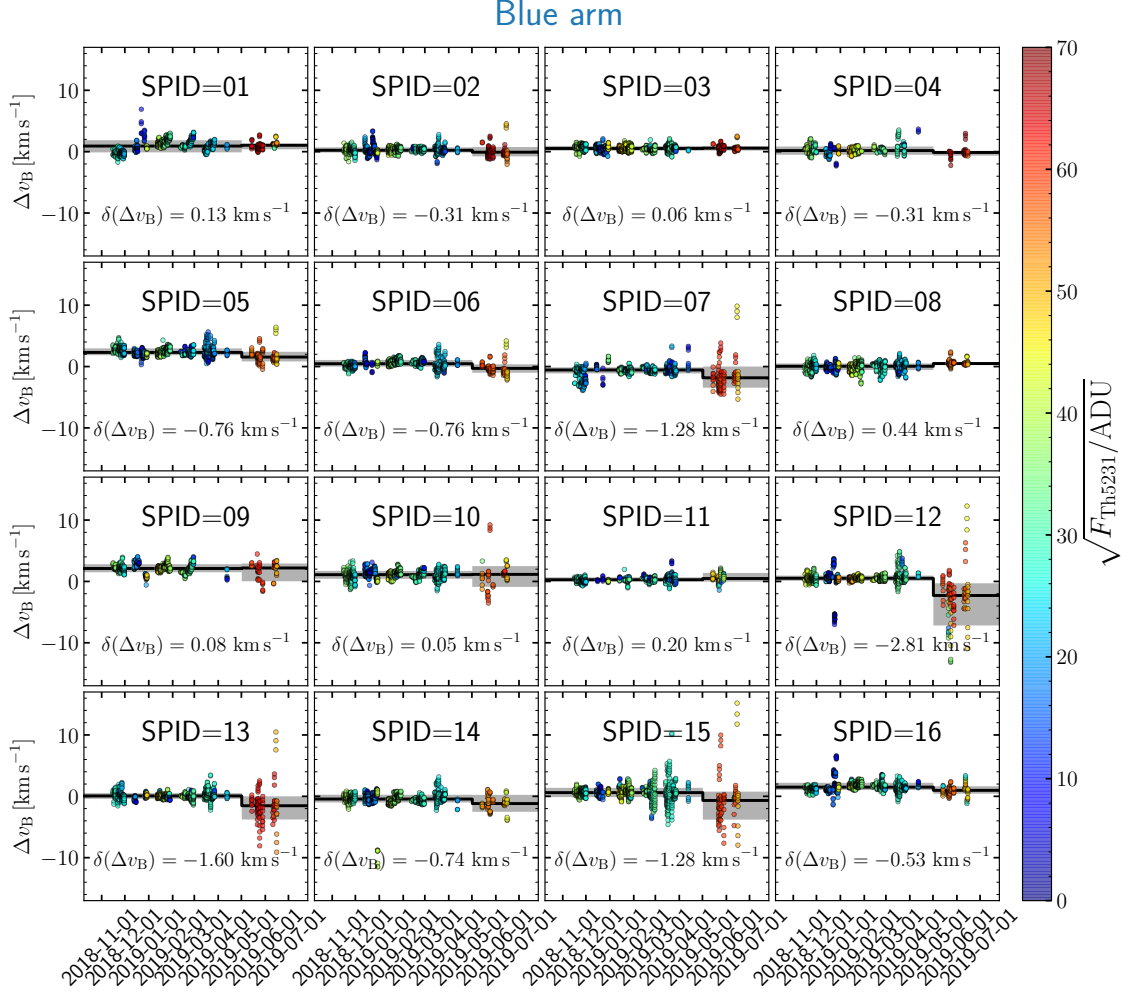


Figure 9. The temporal variance of Δv_B before/after 1 May 2019 for the blue arm. The gray filled areas shows the 16 and 84th percentiles of the Δv_B in the two time intervals, and black solid lines show the medians. Color denotes the square root of the peak flux of the Th5231 line, which can be used as an indicator of SNR. Here the new batch of ThAr lamp also introduce RVZP variance.

indicates the stability of wavelength calibration, i.e., the dispersion of $\Delta v_{i,j,k}$ in SEU $\{i,j\}$, $\Delta v_{i,j}$ is the RVZP correction value of SUE $\{i,j\}$ which is a free variable to be solved, $\bar{v}_{\text{,obs}}$ and $\sigma_{\text{,obs}}$ are the median and scatter of of the (RVZP-corrected) measured radial velocities of the star $\{i,j,k\}$ in other SEUs, Λ_1 and Λ_2 are the regularization parameters of the two terms. In this scheme, the first term guarantees that the absolute scale of our RVZP-corrected RVs is close to that of *Gaia* DR2, while the second term makes use of multiple exposures and guarantees that the relative RVZPs are self-consistent. We set $\Lambda_1 = \Lambda_2 = 1$ so that the final correction of each SEU is determined as an average of the two effects. Then the vector $\Delta \mathbf{v}$ is determined by minimizing the cost function f , i.e., $\Delta \mathbf{v} = \arg \min f$. This algorithm

can be implemented by minimizing

$$\begin{aligned}
 f_{i,j}(\Delta v_{i,j}) = & \Lambda_1 \sum_k \frac{|v_{i,j,k,\text{obs}} + \Delta v_{i,j} - v_{i,j,k,\text{GAIA}}|}{\sqrt{\sigma_{\text{min}}^2 + \sigma_{i,j,k,\text{obs}}^2 + \sigma_{i,j,k,\text{GAIA}}^2}} \\
 & + \Lambda_2 \sum_k \frac{|v_{i,j,k,\text{obs}} + \Delta v_{i,j} - \bar{v}_{\text{,obs}}|}{\sqrt{\sigma_{\text{min}}^2 + \sigma_{i,j,k,\text{obs}}^2 + \sigma_{\text{,obs}}^2}}
 \end{aligned} \tag{4}$$

for each SEU $\{i,j\}$ sequentially and iteratively, where the $\Delta v_{i,j}$ is the RVZP correction value for SUE $\{i,j\}$. Therefore, the problem is to solve the vector $\Delta \mathbf{v}$ which has an N_{SEU} elements where N_{SEU} is the number of related SEUs. We claim that the $\Delta \mathbf{v}$ is determined when the L_∞ norm of the difference between the solutions in l th and $(l+1)$ th iteration is less than a specified value,

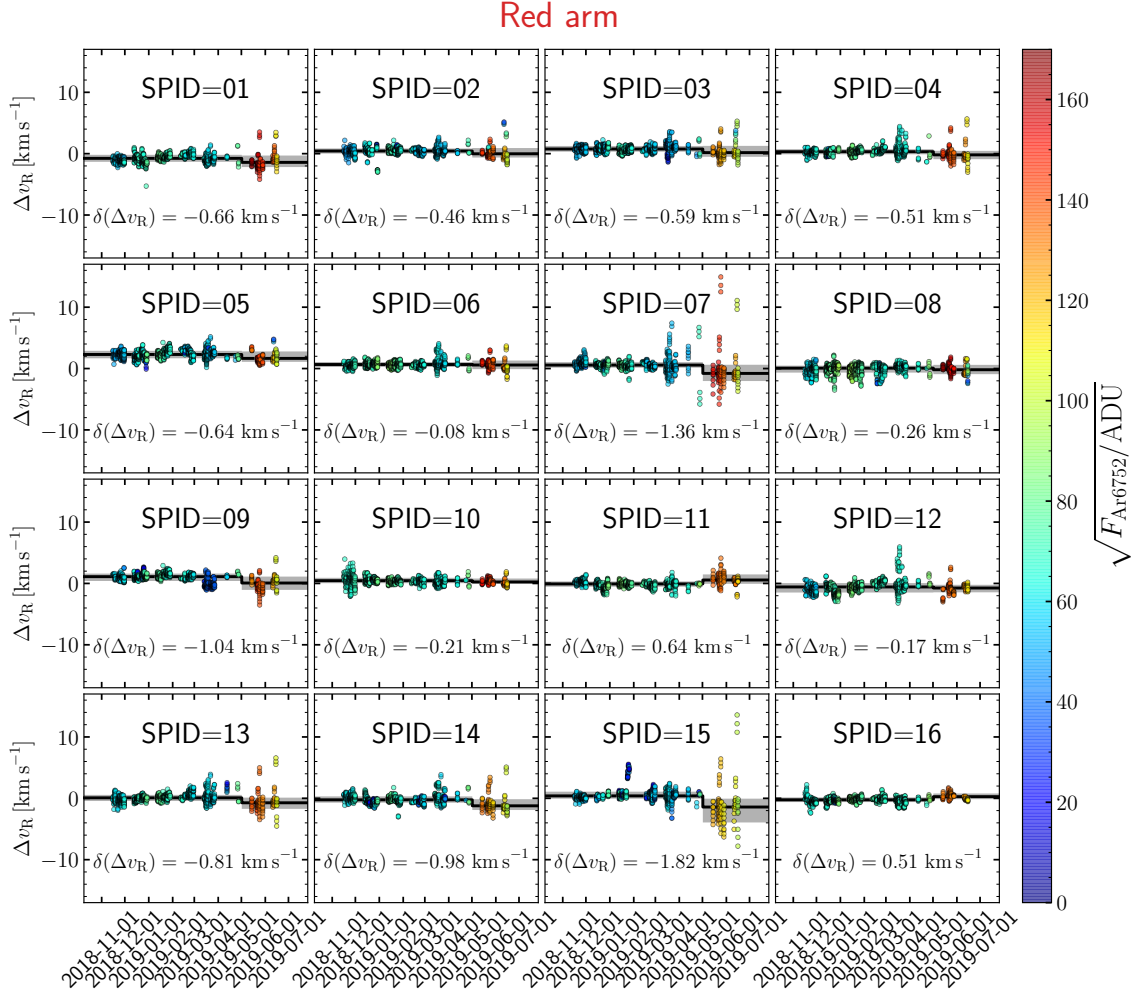


Figure 10. The same figure as Figure 9 but for red arm (Δv_R). Color denotes the square root of the peak flux of Ar6752 line.

i.e., $\max(|\Delta \mathbf{v}_l - \Delta \mathbf{v}_{l+1}|) < \epsilon$, where ϵ is the tolerance and is set to 0.075 km s^{-1} .

The SEUs with RVZP correction values $|\Delta v_{i,j}| > 50 \text{ km s}^{-1}$ or associated uncertainties $\sigma_{\Delta v_{i,j}} > 10 \text{ km s}^{-1}$ (see Section 4.5) are excluded in the iteration. These results are generally because (1) *Gaia* DR2 objects are ≤ 10 (2) spectral SNRs are too low (3) bad spectra due to saturation or instrumental problems. We do not think for these SEUs our scheme and assumptions are valid, so we only keep their initial guesses of $\Delta v_{i,j}$ (see Section 4.4) and their uncertainties (see Section 4.5) in our catalog (see Section 6).

4.4. Tricks to Accelerate the Algorithm

Several tricks are used to accelerate the algorithm. The first trick is to get a good initial estimation of $\Delta \mathbf{v}$. A good approximation can be made by ignoring the second term in Eq. (4), so that with *Gaia* DR2 RVs we

can roughly estimate $\Delta v_{i,j}$ by minimizing

$$f_{i,j,\text{init}}(\Delta v_{i,j}) = \sum_k \frac{|v_{i,j,k,\text{obs}} + \Delta v_{i,j} - v_{i,j,k,\text{GAIA}}|}{\sqrt{\sigma_{\text{min}}^2 + \sigma_{i,j,k,\text{obs}}^2 + \sigma_{i,j,k,\text{GAIA}}^2}}. \quad (5)$$

We note that if an SEU has only a few objects common with the *Gaia* catalog, the estimation is risky. Therefore, we require that an SEU at least have 10 objects common with *Gaia* DR2 to proceed otherwise we calculate the initial guess $\Delta v_{i,j,\text{init}}$ but exclude this SEU in the iteration process.

The second trick is to cut down N_{SEU} by separating physically detached SEUs, which fastens the index evaluation in each iteration. In the Eq. (3) and (4), the second terms contain cross terms, meaning that when solving the N_{SEU} elements, an iteration process is needed to guarantee that the solution of $\Delta \mathbf{v}$ is stable. However, the evaluation of indices is computationally expensive when the N_{SEU} grows. Therefore, before performing

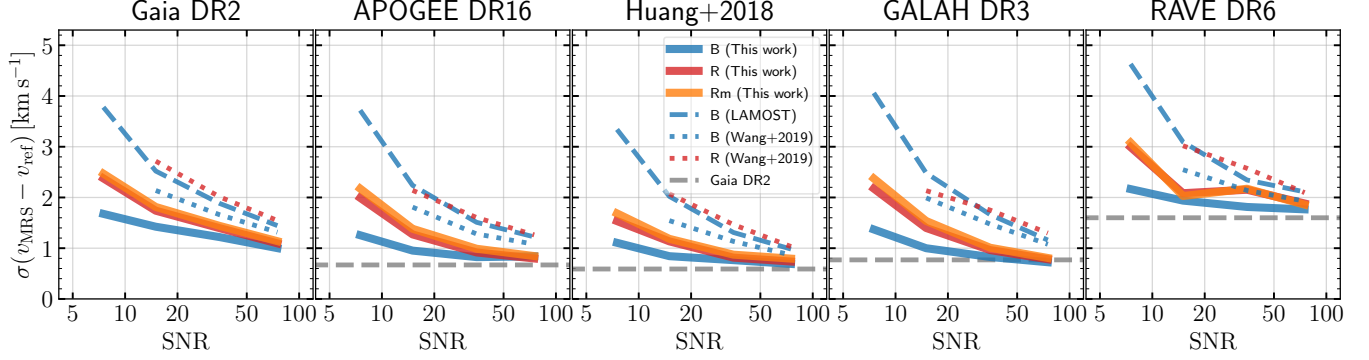


Figure 11. The comparisons of our absolute RVs from LAMOST MRS DR7 (including this work, the LAMOST pipeline, and Wang et al. 2019) with other datasets, i.e., *Gaia* DR2 (Katz et al. 2019), APOGEE DR16 (Column `VHELIO_AVG`, Jönsson et al. 2020), RV standard stars from Huang et al. (2018), GALAH DR3 (Column `rv_galah`, Buder et al. 2020), and RAVE DR6 (Column `hrv_sparv`, Steinmetz et al. 2020b). The scatters (σ s) are estimated using Gaussian fitting method.

the optimization process, physically detached sky areas can be separated, so that the many index evaluation processes can be accelerated by cutting down the array sizes. We group the pointings of LAMOST MRS DR7 using a friends-of-friends algorithm with a 5-degree linking length which is double of the radius of the field-of-view of LAMOST in case of any possible common stars between them. Eventually, 137 groups are obtained, as shown in Figure 6. Initial guesses of Δv for each SEU is made by optimizing the cost function Eq. (3) for each group of plates.

In practice, we find that if the ϵ is too small, there is the possibility that the Δv jumps back and forth between two solutions and does not converge. Further analysis shows that this is an optimization method related problem (we used the Nelder-Mead solver, changing it to the Powell solver does not solve the problem but the two solutions are different). We guess that this might due to the numerical problem of the optimization routine. To avoid such a situation, we then added random processes into the algorithm, i.e., if in l th iteration the solution is Δv_l and after looping over all related SEUs the solution is $\Delta v_{l,\text{opt}}$, we evaluate the $l+1$ th solution by $\Delta v_{l+1} = \eta(\Delta v_{l,\text{opt}} - \Delta v_l) + \Delta v_l$, where the η is a *learning rate* randomly generated between η_0 and η_1 . We set $\eta_0 = 0.5$, $\eta_1 = 1.0$, and $\epsilon = 0.075$, considering the expectation of η is 0.75, the effective tolerance of our solution of Δv is 0.10 km s^{-1} , which is acceptable when compared to the typical precision of measured radial velocities (e.g., $\sim 1.5 \text{ km s}^{-1}$ reported by Wang et al. 2019).

Finally, the RVZP corrections for all the 137 groups of pointings converge after several tens of iterations with a Dell Precision R740 workstation with 2 Intel Xeon Platinum 8260 CPUs (2.40GHz), among which the longest

solution takes ~ 10 hours. Compared to the computational cost of RV measurements using CCF for 3.8 million spectra including blue and red arms (~ 1 week on the same machine), computing the RVZPs is quite fast.

4.5. Uncertainty Estimation

Rigorous uncertainties are very difficult to obtain for our RVZP corrections. The uncertainties of the RVZP correction values consists of two parts, namely the tolerance in the iteration process and the formal error. The tolerance is $\epsilon = 0.1 \text{ km s}^{-1}$ as mentioned above. For the latter part, based on the discussion presented in Appendix B, we use the 16th and 84th percentiles to construct a fiducial error of our RVZP correction values $\Delta v_{i,j}$ divided by an empirical correction ξ to construct the formal error. Hence, the total uncertainties of the RVZP correction values are evaluated via

$$\sigma_{\Delta v_{i,j}}^2 = \left(\frac{q84_{i,j} - q16_{i,j}}{2\xi\sqrt{N_{i,j}}} \right)^2 + \epsilon^2, \quad (6)$$

where i, j index the SEUs, $q16$ and $q84$ denote the 16th and 84th percentiles of the residuals of the *Gaia* DR2 RVs and the RVZP-corrected LAMOST MRS RVs, the $N_{i,j}$ is the number of *Gaia* DR2 objects with RVs, and ξ is the empirical correction factor for small number statistics.

5. RESULTS AND VALIDATION

In total, we have measured RVs from 3 181 157/3 723 934 single-exposure blue/red arm spectra in LAMOST MRS DR7 with SNR higher than 5. For 36 301/37 122/37 122 (B/R/Rm) out of 37 624 SEUs, we have successfully derived initial values of the RVZPs. After eliminating the bad SEUs with criteria described at the end of Section 4.3, we estimate the final RVZPs

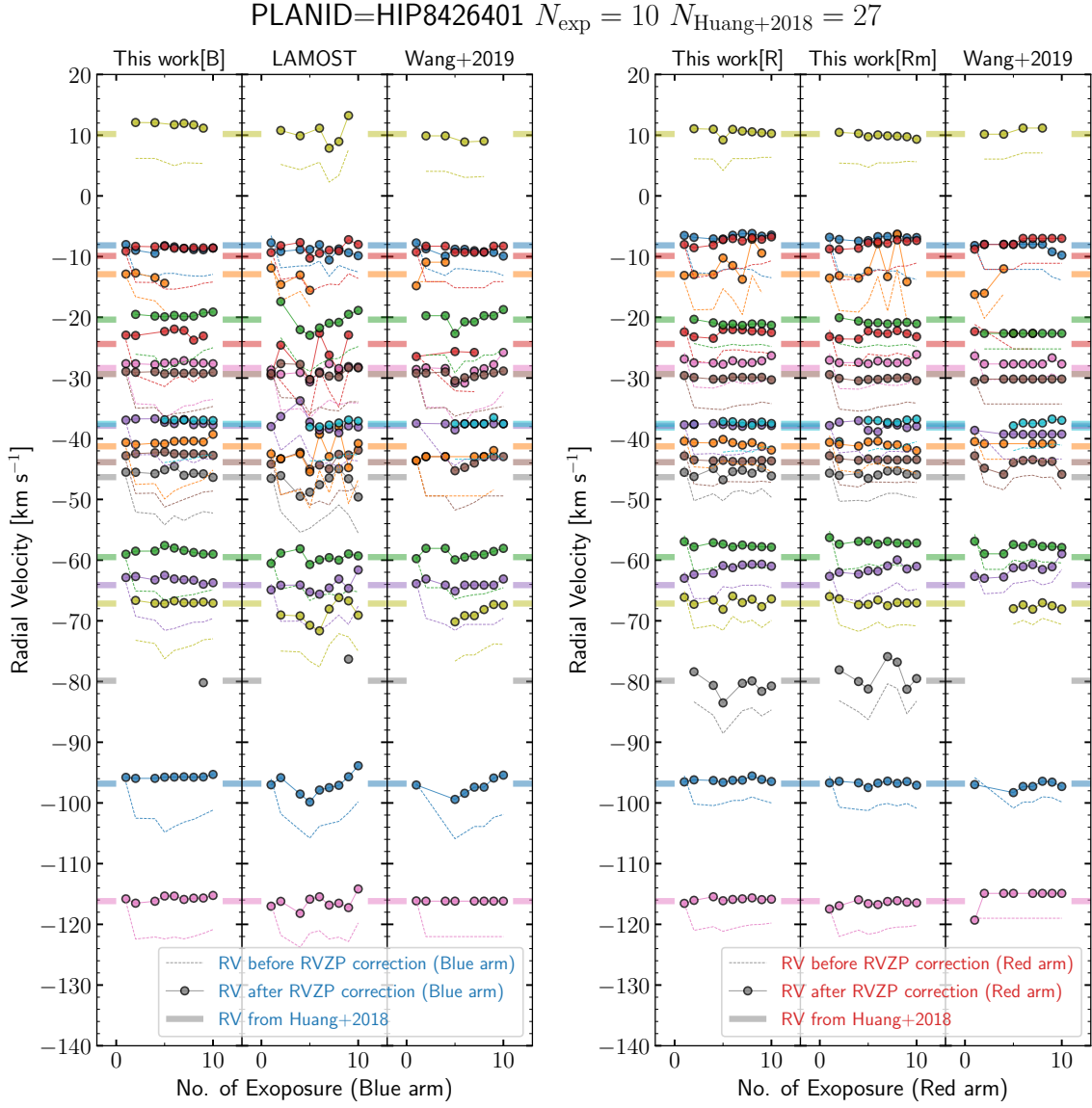


Figure 12. A comparison of the RVs of standard stars observed in LAMOST MRS DR7 (planid=HIP8426401) determined in this work, the LAMOST and Wang et al. (2019). Each color represents a unique RV standard star. The thick ticks show their RVs from Huang et al. (2018), the dashed lines show RVs before RVZP corrections, and the circles connected by solid lines show the RVZP-corrected RVs. The first exposure is on Apr. 2018 and calibrated with Sc lamp, so the correction value is quite different from those of other exposures.

for 33 073/35 207/35 199 (B/R/Rm) SEUs which cover 2 985 015/3 631 023/3 629 895 B/R/Rm RVs. Roughly, the percentages of coverage are 87.9/93.6/93.6% for B/R/Rm in terms of SEUs and 93.8/97.5/97.5% for B/R/Rm in terms of RVs.

5.1. The Temporal Variation of RVZPs

In Figure 7, we present the $\Delta v_{i,j}$ for each SEU for Sc and ThAr arc lamps versus date. The Sc lamp was in use until Oct. 2018, after when it is totally replaced by ThAr lamp. The mean uncertainties of Δv_B , Δv_R and Δv_{Rm} are all $\sim 0.38 \text{ km s}^{-1}$ which are quite good.

The median uncertainty is even 20% less. The Δv_B and Δv_R have different patterns while the Δv_R and Δv_{Rm} are very similar. In Figure 8 we show the distribution of the Δv_B , Δv_R and Δv_{Rm} of the SEUs solved. The μ here is estimated using the median, and σ estimated using $(q_{84} - q_{16})/2$. The μ s are 0.49 and 6.47 km s^{-1} for ThAr and Sc lamp in the blue arm, while in the red arm they are 0.26 and 4.91 km s^{-1} , respectively. The σ s are 1.07 and 1.06 km s^{-1} for ThAr and Sc lamp in blue arm, and in red arm are 0.85 and 0.68 km s^{-1} . Generally, the different systematics for Sc and ThAr lamp-calibrated data, which is consistent with (Wang et al.

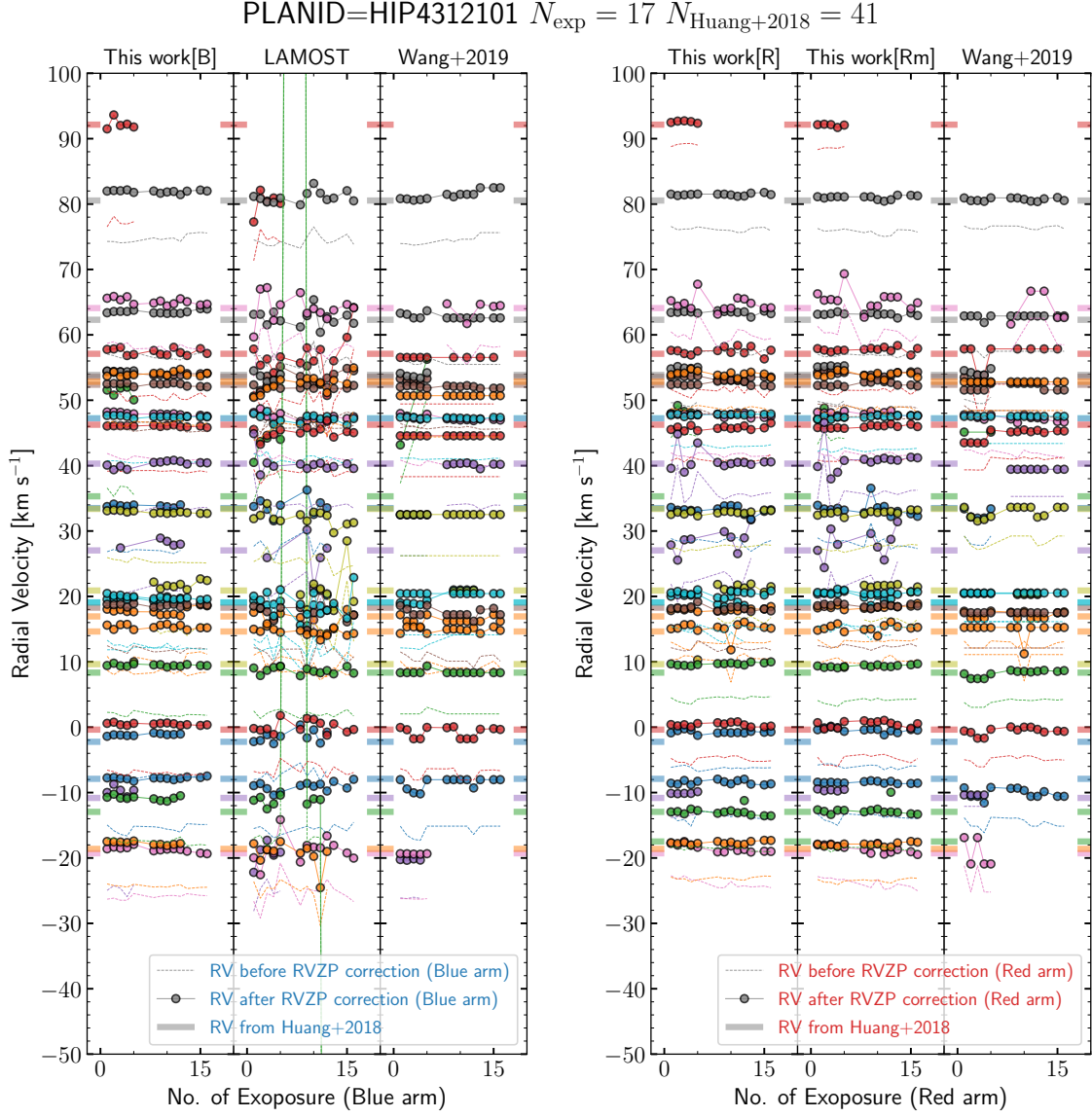


Figure 13. The same figure as Figure 12 but for `planid=HIP4312101`.

2019). Despite the large systematics, we find that the precision of the Sc lamp calibrated data is no worse than those calibrated by ThAr lamp. The Rm results are very similar to that of R, except their μs have a 0.3 km s^{-1} difference. We note that this is reasonable considering that the systematics vary with wavelength as shown in Ren et al. (2020). In addition, ~ 4000 single-exposure spectra calibrated using Ne lamp are also found in DR7 v1.1. We confirm that the Ne lamp is used to calibrate the LRS spectra and these mistakenly calibrated data will be removed in DR7 v2 (the internationally public version), so we exclude these data in the following analysis.

It is clear that the RVZPs are reasonably stable except after ~ 1 May 2019, which seems to be correlated

with the arc lamp exposure flux⁴. We plot the Δv for each spectrograph for the time interval with available arc lamp intensity in Figure 9 and 10. Since our mean uncertainty of $\Delta v_{i,j}$ is 0.38 km s^{-1} , we regard the $\Delta v_{i,j}$ larger than 1 km s^{-1} as significant values, including the 7, 12, 13, 15th spectrographs of the blue arm and 7, 9, 15th spectrographs of the red arm. It is currently not sure whether these shifts are due to that the new ThAr lamps are brought into use at around 1 May 2019 or some other issues induced in the maintenance. Probably

⁴ We also get access to the peak flux of Th5231 and Ar6752 of each ThAr lamp exposure since Nov. 2018 which are not included in the formal data release.

in DR8, with the RVZP data in a longer time baseline we can address the problem.

5.2. Validating with Other Datasets

We also validate our RVs with the stars common in other datasets, namely, the *Gaia* DR2 (Katz et al. 2019), APOGEE DR16 (Column VHELIO.AVG, Jönsson et al. 2020), RV standard stars from Huang et al. (2018), GALAH DR3 (Column rv_galah, Buder et al. 2020), and RAVE DR6 (Column hrv_sparv, Steinmetz et al. 2020b). The mean μ and scatter σ derived from Gaussian fitting to the residuals are tabulated in Table 2 and shown as functions of SNR in Figure 11. Also shown are the results of the LAMOST pipeline and Wang et al. (2019). Note that, in DR7 v1.1, the LAMOST pipeline only provides two RVs measured from the blue arm using ELODIE empirical templates (Moultaka et al. 2004) and ATLAS9 synthetic templates (Castelli & Kurucz 2003), respectively. In the next version of DR7 (v1.2) and future data releases, the RVs using ELODIE templates will be removed, and the RVs based on ATLAS9 will be provided for both blue and red arms for better performance. Therefore, we use their calibrated RVs of blue arms based on ATLAS9 templates in our comparison (Column rv_ku1). The Wang et al. (2019) catalog is a subset of ours (including data taken during the first one year and a half with SNR cut at 10). The spectra without our measurements (i.e., either $\text{SNR} < 5$ or Δv is invalid) are excluded in this comparison, so that it is fair to the other two RV sources. At high SNR end (50 to 100), we found the standard deviations derived from Gaussian fitting for our results can reach 1.00/1.10, 0.84/0.80, 0.69/0.74, 0.72/0.78, and 1.77/1.88 km s^{-1} with respect to the *Gaia* DR2, APOGEE DR16, Huang et al. (2018), GALAH DR3, and RAVE DR6 in blue/red arm. The common stars among LAMOST MRS DR7, *Gaia* DR2 and the other four reference sets are used to calculate the fiducial accuracy of *Gaia* DR2. At the high-SNR end ($50 < \text{SNR} < 100$), the LAMOST MRS gets close to the performance of *Gaia* DR2 (see Figure 11). Note that, in our algorithm, the *Gaia* DR2 RVs are used as a reference set, so the comparison with *Gaia* DR2 is not an independent validation. These results of the comparisons are quite fascinating. At high-SNR end, we outperform Wang et al. (2019) and LAMOST pipeline by $\sim 20\%$ and 30% , respectively, according to the blue arm results compared to APOGEE DR16. At low-SNR end (10 to 20), this advantage increases to 58% and 47% , indicating that our algorithm of RV measurements and RVZP determinations are quite efficient. Since the Huang et al. (2018) sample is from APOGEE DR14, the comparison to Huang et al. (2018)

has a 0.4 km s^{-1} systematic bias which does not exist in our comparison to APOGEE DR16. This may be due to the update of the APOGEE data release. The GALAH DR3 has a 0.23 km s^{-1} systematic bias compared to *Gaia* DR2. The comparison with RAVE DR6, whose spectral resolution is the same as the LAMOST MRS but lower than *Gaia*-RVS, APOGEE and GALAH, shows a large scatter but is still reasonable.

5.3. The Self-consistency

Besides the precision, a check on the self-consistency is necessary before using RVs in time-domain research. As a demonstration, in Figure 12 and 13 we validate the temporal RV variations of the standard stars (whose RVs are assumed invariant) from Huang et al. (2018) in two pointings, namely, planid=HIP8426401 and HIP4312101, which have 10 and 17 exposures and contain 27 and 41 RV standard stars, respectively. It is obvious that the RVs from the LAMOST pipeline show large fluctuations, which is as expected from the comparison in Section 5.2. It turns out that for many stars, the RVs of multiple exposures from Wang et al. (2019) catalog have exactly the same values. This is due to the failure of their Gaussian fitting process and then they fall back on best estimation from the 1 km s^{-1} RV grid, which is a defect in the algorithm. By comparing the measured RVs and the RVZP-corrected RVs, we find that the RVZP-corrected RVs are much cleaner, indicating that the RVs do benefit from our algorithm for $\Delta v_{i,j}$ determination. The LAMOST pipeline and Wang et al. (2019) assume that the RVZP for a spectrograph is static, so that the RVZP corrections are basically a shift of the RVs.

To quantify the performance in self-consistency, we select RV standard stars from Huang et al. (2018) with at least 8 exposures have valid RVZP-corrected RVs in our catalog and calculated their standard deviation empirically corrected for the small-number-statistic effect which is discussed in Appendix B. The cumulative distribution function (CDF) of the standard deviations is shown in Figure 14. The RVs measured from blue arm (B) shows the best consistency while those from red arm (R) and H α -masked red arm (Rm) follow. By calculating the 50th, 90th and 95th percentiles of the CDFs for the blue arm results, we find our RVs have significant advantages over the LAMOST pipeline, namely 16.5%, 35.5% and 37.5% better, while Wang et al. (2019) is at nearly the same level as LAMOST pipeline. This reveals the excellent self-consistency of our RVs in the time-domain analysis. Note that, these estimations of advantages are very conservative due to the facts such as Wang et al. (2019) dataset cut SNR at 10 but LAMOST

Table 2. Compare the LAMOST MRS RVs to other datasets

SNR	Ref. Dataset	This Work			LAMOST	Wang et al. (2019)		<i>Gaia</i> DR2
		Blue arm	Red arm	H α masked	Blue arm	Blue arm	Red arm	RVS
<i>Gaia</i> DR2	5 < SNR < 10	$N = 166218$ $\mu = -0.02$ $\sigma = 1.68$	$N = 89032$ $\mu = -0.05$ $\sigma = 2.38$	$N = 89009$ $\mu = -0.07$ $\sigma = 2.47$	$N = 166218$ $\mu = -0.56$ $\sigma = 3.78$	$N = 0$ – –	$N = 0$ – –	– – –
	10 < SNR < 20	$N = 301963$ $\mu = -0.04$ $\sigma = 1.42$	$N = 164068$ $\mu = -0.10$ $\sigma = 1.74$	$N = 164010$ $\mu = -0.10$ $\sigma = 1.81$	$N = 301963$ $\mu = -0.53$ $\sigma = 2.52$	$N = 209446$ $\mu = -0.55$ $\sigma = 2.14$	$N = 26195$ $\mu = -0.59$ $\sigma = 2.72$	– – –
	20 < SNR < 50	$N = 572355$ $\mu = -0.03$ $\sigma = 1.22$	$N = 531044$ $\mu = -0.07$ $\sigma = 1.39$	$N = 530913$ $\mu = -0.08$ $\sigma = 1.44$	$N = 572355$ $\mu = -0.44$ $\sigma = 1.88$	$N = 389277$ $\mu = -0.46$ $\sigma = 1.66$	$N = 313059$ $\mu = -0.66$ $\sigma = 2.01$	– – –
	50 < SNR < 100	$N = 270880$ $\mu = 0.00$ $\sigma = 1.00$	$N = 497328$ $\mu = -0.00$ $\sigma = 1.10$	$N = 497126$ $\mu = -0.01$ $\sigma = 1.14$	$N = 270880$ $\mu = -0.33$ $\sigma = 1.45$	$N = 180183$ $\mu = -0.35$ $\sigma = 1.32$	$N = 322647$ $\mu = -0.58$ $\sigma = 1.55$	– – –
APOGEE DR16	5 < SNR < 10	$N = 35352$ $\mu = 0.22$ $\sigma = 1.26$	$N = 23362$ $\mu = 0.08$ $\sigma = 1.99$	$N = 23354$ $\mu = 0.06$ $\sigma = 2.17$	$N = 35352$ $\mu = -0.39$ $\sigma = 3.72$	$N = 0$ – –	$N = 0$ – –	$N = 28155$ $\mu = 0.02$ $\sigma = 0.67$
	10 < SNR < 20	$N = 49482$ $\mu = 0.13$ $\sigma = 0.95$	$N = 38971$ $\mu = 0.08$ $\sigma = 1.27$	$N = 38987$ $\mu = 0.02$ $\sigma = 1.38$	$N = 49482$ $\mu = -0.41$ $\sigma = 2.24$	$N = 33297$ $\mu = -0.46$ $\sigma = 1.81$	$N = 4781$ $\mu = -0.47$ $\sigma = 2.14$	
	20 < SNR < 50	$N = 80556$ $\mu = 0.06$ $\sigma = 0.82$	$N = 87168$ $\mu = 0.06$ $\sigma = 0.92$	$N = 87159$ $\mu = 0.03$ $\sigma = 0.99$	$N = 80556$ $\mu = -0.41$ $\sigma = 1.51$	$N = 52872$ $\mu = -0.43$ $\sigma = 1.28$	$N = 48104$ $\mu = -0.49$ $\sigma = 1.60$	
	50 < SNR < 100	$N = 41479$ $\mu = -0.04$ $\sigma = 0.84$	$N = 73363$ $\mu = 0.04$ $\sigma = 0.80$	$N = 73350$ $\mu = 0.04$ $\sigma = 0.85$	$N = 41479$ $\mu = -0.41$ $\sigma = 1.22$	$N = 26724$ $\mu = -0.42$ $\sigma = 1.08$	$N = 45191$ $\mu = -0.51$ $\sigma = 1.26$	
Huang et al. (2018)	5 < SNR < 10	$N = 2753$ $\mu = 0.44$ $\sigma = 1.11$	$N = 1659$ $\mu = 0.33$ $\sigma = 1.53$	$N = 1661$ $\mu = 0.36$ $\sigma = 1.69$	$N = 2753$ $\mu = 0.28$ $\sigma = 3.34$	$N = 0$ – –	$N = 0$ – –	$N = 2070$ $\mu = 0.34$ $\sigma = 0.59$
	10 < SNR < 20	$N = 3404$ $\mu = 0.43$ $\sigma = 0.84$	$N = 2890$ $\mu = 0.36$ $\sigma = 1.13$	$N = 2890$ $\mu = 0.36$ $\sigma = 1.18$	$N = 3404$ $\mu = 0.01$ $\sigma = 2.02$	$N = 2316$ $\mu = -0.18$ $\sigma = 1.54$	$N = 161$ $\mu = 0.18$ $\sigma = 2.07$	
	20 < SNR < 50	$N = 5050$ $\mu = 0.42$ $\sigma = 0.76$	$N = 5923$ $\mu = 0.39$ $\sigma = 0.81$	$N = 5920$ $\mu = 0.40$ $\sigma = 0.87$	$N = 5050$ $\mu = 0.01$ $\sigma = 1.31$	$N = 3352$ $\mu = -0.05$ $\sigma = 1.13$	$N = 2938$ $\mu = 0.10$ $\sigma = 1.47$	
	50 < SNR < 100	$N = 2507$ $\mu = 0.38$ $\sigma = 0.69$	$N = 4917$ $\mu = 0.44$ $\sigma = 0.74$	$N = 4916$ $\mu = 0.47$ $\sigma = 0.79$	$N = 2507$ $\mu = 0.06$ $\sigma = 0.98$	$N = 1711$ $\mu = 0.05$ $\sigma = 0.87$	$N = 3127$ $\mu = -0.08$ $\sigma = 1.03$	
GALAH DR3	5 < SNR < 10	$N = 30272$ $\mu = 0.32$ $\sigma = 1.37$	$N = 17317$ $\mu = 0.26$ $\sigma = 2.18$	$N = 17271$ $\mu = 0.22$ $\sigma = 2.37$	$N = 30272$ $\mu = -0.25$ $\sigma = 4.06$	$N = 0$ – –	$N = 0$ – –	$N = 8778$ $\mu = 0.23$ $\sigma = 0.77$
	10 < SNR < 20	$N = 42242$ $\mu = 0.27$ $\sigma = 1.00$	$N = 32885$ $\mu = 0.29$ $\sigma = 1.40$	$N = 32768$ $\mu = 0.23$ $\sigma = 1.54$	$N = 42242$ $\mu = -0.20$ $\sigma = 2.48$	$N = 29780$ $\mu = -0.28$ $\sigma = 1.99$	$N = 5135$ $\mu = -0.19$ $\sigma = 2.13$	
	20 < SNR < 50	$N = 52015$ $\mu = 0.26$ $\sigma = 0.83$	$N = 63642$ $\mu = 0.27$ $\sigma = 0.96$	$N = 63593$ $\mu = 0.22$ $\sigma = 1.01$	$N = 52015$ $\mu = -0.10$ $\sigma = 1.66$	$N = 37996$ $\mu = -0.14$ $\sigma = 1.47$	$N = 40401$ $\mu = -0.32$ $\sigma = 1.75$	
	50 < SNR < 100	$N = 18796$ $\mu = 0.24$ $\sigma = 0.72$	$N = 37239$ $\mu = 0.29$ $\sigma = 0.78$	$N = 37239$ $\mu = 0.27$ $\sigma = 0.81$	$N = 18796$ $\mu = -0.07$ $\sigma = 1.16$	$N = 13727$ $\mu = -0.13$ $\sigma = 1.08$	$N = 27296$ $\mu = -0.31$ $\sigma = 1.30$	
RAVE DR6	5 < SNR < 10	$N = 593$ $\mu = 0.53$ $\sigma = 2.17$	$N = 414$ $\mu = 0.93$ $\sigma = 2.99$	$N = 414$ $\mu = 0.77$ $\sigma = 3.08$	$N = 593$ $\mu = 0.13$ $\sigma = 4.63$	$N = 0$ – –	$N = 0$ – –	$N = 1674$ $\mu = 0.33$ $\sigma = 1.60$
	10 < SNR < 20	$N = 1273$ $\mu = 0.47$ $\sigma = 1.94$	$N = 719$ $\mu = 0.50$ $\sigma = 2.08$	$N = 719$ $\mu = 0.37$ $\sigma = 2.03$	$N = 1273$ $\mu = -0.29$ $\sigma = 3.10$	$N = 862$ $\mu = -0.19$ $\sigma = 2.55$	$N = 146$ $\mu = 0.14$ $\sigma = 3.02$	
	20 < SNR < 50	$N = 3343$ $\mu = 0.39$ $\sigma = 1.81$	$N = 2273$ $\mu = 0.62$ $\sigma = 2.15$	$N = 2273$ $\mu = 0.55$ $\sigma = 2.17$	$N = 3343$ $\mu = -0.09$ $\sigma = 2.34$	$N = 2539$ $\mu = -0.16$ $\sigma = 2.14$	$N = 1487$ $\mu = 0.15$ $\sigma = 2.57$	
	50 < SNR < 100	$N = 2332$ $\mu = 0.35$ $\sigma = 1.77$	$N = 3209$ $\mu = 0.41$ $\sigma = 1.88$	$N = 3209$ $\mu = 0.35$ $\sigma = 1.86$	$N = 2332$ $\mu = 0.08$ $\sigma = 2.11$	$N = 1798$ $\mu = 0.05$ $\sigma = 1.93$	$N = 2368$ $\mu = -0.25$ $\sigma = 2.10$	

NOTE—In each cell, we present the number of star (N), the Gaussian fitted systematic bias ($\mu/\text{km s}^{-1}$) and the standard error ($\sigma/\text{km s}^{-1}$) with respect to a specific reference set.

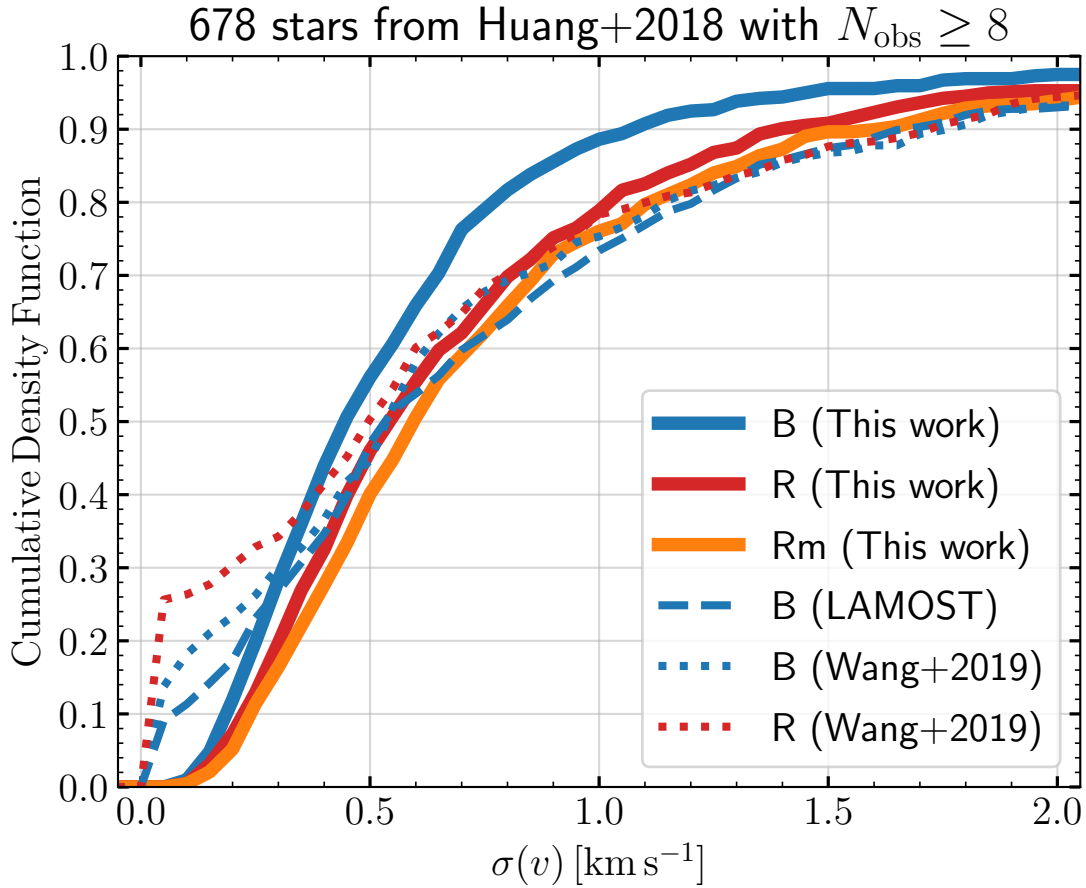


Figure 14. The CDFs of the standard deviations of multiple observations for 678 RV standard stars (Huang et al. 2018) observed in LAMOST MRS DR7. The blue/red/orange color denote the B/R/Rm measurements, and the solid/dashed/dotted lines represent the results of this work/LAMOST/Wang et al. (2019).

Table 3. The comparison of self-consistencies between this work, the LAMOST pipeline and Wang et al. (2019).

Percentile	This Work			LAMOST	Wang et al. (2019)	
	Blue arm	Red arm	H α masked	Blue arm	Blue arm	Red arm
$q = 50\%$	0.45 (16.5%)	0.54	0.59	0.53	0.54 (-0.7%)	0.50
$q = 90\%$	1.07 (35.5%)	1.39	1.61	1.66	1.76 (-5.8%)	1.72
$q = 95\%$	1.45 (37.5%)	1.86	2.10	2.32	2.29 (1.5%)	2.08

NOTE—Each column shows the RV standard deviation for the 678 standard stars at corresponding levels of the CDF. In the parentheses we show the advantages over the LAMOST blue arm results.

and our sample cut at 5. Besides, we do not exclude any of the "exactly the same" RVs from Wang et al. (2019) as readers may find that the CDFs for LAMOST and Wang et al. (2019) jump at around 0 km s^{-1} position.

With the self-consistency performance, we select 10 320 candidate RV standard stars by requiring that in blue arm (B) and red arm (R)

1. their numbers of exposures are at least 8,
2. their absolute RVs have standard deviations (corrected for small number statistics) are less than 1.45 and 1.85 km s^{-1} (corresponding to the 95% level of the CDF, or 95% completeness with respect to Huang et al. 2018),
3. their time baselines are at least longer than 180 days.

These stars can be useful for RV calibration of low-resolution surveys such the LAMOST LRS survey ($R \sim 1800$).

6. DATA PRODUCTS

The data products of this work include

1. a catalog of ~ 3.8 million measured RVs (but 5 million rows for completeness), associated errors and the information of observations for ~ 0.8 million stars (Table 4),
2. a catalog of the $\Delta v_{i,j}$ for B, R, and Rm measurements in each SEU, and their uncertainties corresponding to ~ 3.6 million RVs (Table 5).
3. a catalog of 10 320 candidate RV standard stars with more than 8 exposures and standard deviation less than $1.45/1.86 \text{ km s}^{-1}$ in blue/red arm over a time baseline longer than 180 days (Table 6).

The catalogs can be cross-matched using the columns `spid` and `lmjm`. They will be available with the journal and also at <https://github.com/hypergravity/paperdata> once the paper is accepted.

A few tips: the users who want to correct Doppler effects of their spectra (e.g., Zhang et al. 2020a) should use RVs without RVZP corrections, while the users who want to use absolute RVs can obtain them from our catalog via Eq (2). The uncertainties of the absolute RVs can be evaluated via

$$\sigma_{\text{abs}}^2 = \sigma_{v,\text{obs}}^2 + \sigma_{\text{min}}^2 + \sigma_{\Delta v}^2 + \sigma_{\text{mod}}^2, \quad (7)$$

where $\sigma_{v,\text{obs}}$ is the measurement error, σ_{min} is the wavelength calibration error floor which we can infer from

the comparison to APOGEE DR16 that it is approximately 0.85 km s^{-1} or conservatively 1 km s^{-1} , $\sigma_{\Delta v}$ is the uncertainty of the RVZP, and σ_{mod} is the contribution from the sparsity of the spectral templates (0.10 km s^{-1} for blue arm and 0.20 km s^{-1} for red arm).

7. SUMMARY

In this paper, we measure the RVs from LAMOST Medium-Resolution Survey (MRS) DR7 stellar spectra and determine the RVZPs with the help of *Gaia* DR2 RVs, aiming at making the absolute RVs self-consistent and proper for time-domain analysis. More specifically,

1. we have measured RVs of ~ 3.8 million single-exposure spectra for more than 0.8 million stars obtained from the LAMOST MRS DR7, including the blue arm, red arm (with and without $H\alpha$),
2. we determine the RVZPs exposure by exposure (for 3.6 million spectra) by comparing the measured RVs to the *Gaia* DR2 and multiple MRS exposures using a robust method to a mean precision of 0.38 km s^{-1} ,
3. we find the RVZP vary significantly for some spectrographs before/after 1 May 2019, which confirmed the necessity of our algorithm to determine the RVZPs,
4. we find good agreements in the comparisons of our absolute RVs with APOGEE DR16, RV standard stars (Huang et al. 2018), GALAH DR3, and RAVE DR6, and the precision at $50 < \text{SNR} < 100$ can reach $1.00/1.10$, $0.84/0.80$, $0.69/0.74$, $0.72/0.78$, and $1.77/1.88 \text{ km s}^{-1}$ in the blue/red arm, respectively,
5. we show that our absolute RVs have 16.5, 35.5, and 37.5% better self-consistency at 50%, 90%, and 95% levels of the CDF of standard deviations, respectively, which benefits subsequent time-domain analysis.
6. we select a set of (**Replaced: 9 708** replaced with: **10 320**) candidate RV standard stars whose standard deviations of RVs are less than 1.45 and 1.86 km s^{-1} in the blue arm and red arm, respectively, over a time baseline of at least 180 days.

The algorithms and results presented in this work will be used in the subsequent works on spectroscopic binaries (Xiong et al. in prep., Zhang et al. in prep.).

The LAMOST MRS DR7 v1.2 and v1.3 have been released. We confirm that, in DR7 v1.2/1.3 the spectra are the same as v1.1 but catalogs and parameters

Table 4. The 3.8 million RVs obtained from the LAMOST MRS DR7 (v1.1).

OBSID	LMJM	BJD	PLANID	SPID	FIBERID	RA	DEC	SNRB	SNRR	LAMPB	LAMPB
(1)	(2)	(3)	(4)	(5)	(6)	deg	deg	(9)	(10)	(11)	(12)
588902003	83556146	2458025.2773235	HIP507401	2	3	15.3672776	4.0094024	25.2	44.7	sc	sc
588902003	83556132	2458025.2679947	HIP507401	2	3	15.3672776	4.0094024	29.8	52.1	sc	sc
588902003	83556119	2458025.2587006	HIP507401	2	3	15.3672776	4.0094024	30.6	52.4	sc	sc

V_B	VERR_B	TEFF_B	CCFMAX_B	V_R	VERR_R	TEFF_R	CCFMAX_R	V_RM	VERR_RM	TEFF_RM	CCFMAX_RM
km s ⁻¹	km s ⁻¹	K		km s ⁻¹	km s ⁻¹	K		km s ⁻¹	km s ⁻¹	K	
(13)	(14)	(15)	(16)	(17)	(18)	(19)	(20)	(21)	(22)	(23)	(24)
-10.847	0.140	4976.0	0.921	-8.859	0.158	5813.7	0.829	-8.847	0.176	5813.7	0.815
-10.628	0.078	4976.0	0.929	-8.637	0.157	4976.0	0.845	-8.859	0.191	5813.7	0.832
-10.735	0.090	4976.0	0.931	-8.297	0.183	4976.0	0.850	-8.599	0.144	5813.7	0.842

NOTE—Column 1 is the observational ID in LAMOST, Column 2 is the local Modified Julian Minute (1440 × the local Modified Julian Date) of the beginning of exposure which is an 8-bit integer assigned to each exposure, Column 3 is the barycentric Julian Day of the middle of exposure, Column 4 is the plan ID, Column 5 is the spectrograph ID, Column 6 is the fiber ID, Column 7-8 are equatorial coordinates, Column 9-10 are the SNRs in blue and red arms, Column 11-12 are the calibration arc lamp. Column 13-16 are the measured RV, associated measurement error, the effective temperature of the best-match template, the maximum of the CCF, respectively, for the blue arm. Column 17-20 and 21-24 are for the red arm and H α -masked red arm. We refer readers to <http://dr7.lamost.org/v1.1/doc/mr-data-production-description> for detailed explanations of the Column 1-6.

will have some changes⁵⁶. Therefore, our results can be cross-matched with the v1.2/1.3 catalogs directly. And we will release a new version of RVs on github once DR8 is released. On the other hand, since *Gaia* eDR3 is the same as in DR2 but with moderate filtering, our absolute RVs should be consistent with *Gaia* eDR3. In future LAMOST MRS data releases, we will update our RVs using the most recent *Gaia* RVs as reference set.

ACKNOWLEDGMENTS

BZ thanks Qin Lai, Feng Luo, Dr. Rui Wang, Dr. Hai-Bo Yuan, Prof. Jian-Jun Chen, Prof. Hao-Tong Zhang, Prof. A-Li Luo, Prof. Jian-Rong Shi for constructive discussion and generous help. BZ also thanks the support from the LAMOST FELLOWSHIP fund.

JNF acknowledges the support from the National Natural Science Foundation of China (NSFC) through the grants 11833002, 12090042 and 12090040.

This work is supported by National Key R&D Program of China No. 2019YFA0405500. C.L. thanks the National Natural Science Foundation of China (NSFC) with grant No. 11835057.

This work is supported by Chinese Space Station Telescope (CSST) pre-research projects of *Key Problems in Binaries and Chemical Evolution of the Milky Way and its Nearby Galaxies*, the National Natural Science Foundation of China (No. U1931209).

W.Z. is supported by the Fundamental Research Funds for the Central Universities.

The authors also thank the reviewer of this paper for the patience and constructive comments during these days.

The LAMOST FELLOWSHIP is supported by Special Funding for Advanced Users, budgeted and administrated by Center for Astronomical Mega-Science, Chinese Academy of Sciences (CAMS). This work is supported by Cultivation Project for LAMOST Scientific Payoff and Research Achievement of CAMS-CAS.

Guoshoujing Telescope (the Large Sky Area Multi-Object Fiber Spectroscopic Telescope LAMOST) is a National Major Scientific Project built by the Chinese Academy of Sciences. Funding for the project has been provided by the National Development and Reform Commission. LAMOST is operated and managed by the National Astronomical Observatories, Chinese Academy of Sciences.

Facilities: LAMOST

Software: `laspec`(Zhang 2020a), `regli`(Zhang 2020b), `berliner`(Zhang 2020c), `scikit-learn`(Pedregosa et al. 2012), `astropy`(Astropy Collaboration et al. 2018)

Table 5. The RVZP correction values for LAMOST MRS DR7 (v1.1).

PLANID	LMJM	SPID	DV0_B	N_B	DV_B	NF1_B	NF2_B	NO_MED_B	NO_MAX_B	NO_MIN_B	DVERR_B
			km s ⁻¹		km s ⁻¹						
(1)	(2)	(3)	(4)	(5)	(6)	(7)	(8)	(9)	(10)	(11)	(12)
HIP9645901	83555758	2	6.412	156	6.353	111	82	7	47	3	0.188
HIP9645901	83555758	3	8.004	170	7.998	132	168	3	46	0	0.178
HIP9645901	83555758	4	6.126	159	6.128	127	158	3	7	2	0.213

DV0_R	N_R	DV_R	NF1_R	NF2_R	NO_MED_R	NO_MAX_R	NO_MIN_R	DVERR_R
km s ⁻¹		km s ⁻¹						
(13)	(14)	(15)	(16)	(17)	(18)	(19)	(20)	(21)
5.012	159	4.886	113	88	7	47	3	0.183
3.921	170	3.905	132	170	3	46	3	0.169
3.738	163	3.706	129	163	3	7	3	0.192

DV0_RM	N_RM	DV_RM	NF1_RM	NF2_RM	NO_MED_RM	NO_MAX_RM	NO_MIN_RM	DVERR_RM
km s ⁻¹		km s ⁻¹						
(22)	(23)	(24)	(25)	(26)	(27)	(28)	(29)	(30)
5.176	159	5.056	113	88	7	47	3	0.190
3.958	170	3.954	132	170	3	46	3	0.195
3.818	163	3.830	129	163	3	7	3	0.202

NOTE—Column 1 is the plan ID, Column 2 is the local Modified Julian Minute, Column 3 is the spectrograph ID. Column 4-12 are the initial RVZP correction value ($\Delta v_{i,j,\text{init}}$), number of objects, final RVZP correction value ($\Delta v_{i,j}$), number of objects for the first term of the Eq. (4), number of objects for the second term of the Eq. (4), the median number of exposures, the maximum number of exposures, the minimum number of exposures, the estimated uncertainty, respectively, for the blue arm. Column 13-21 and 22-30 are for the red arm and H α -masked red arm, respectively.

Table 6. The selected candidates of RV standard stars from LAMOST MRS DR7 (v1.1).

RA	DEC	RVMED_B	RVSTD_B	NEXP_B	TBL_B	RVMED_R	RVSTD_R	NEXP_R	TBL_R
deg	deg	km s ⁻¹	km s ⁻¹		day	km s ⁻¹	km s ⁻¹		day
(1)	(2)	(3)	(4)	(5)	(6)	(7)	(8)	(9)	(10)
15.367275	4.009401	-4.644	0.350	47	427.896	-4.215	0.358	47	427.896
15.306525	3.796851	15.830	1.027	30	452.830	16.281	1.063	33	452.830
15.541034	3.710481	20.450	0.884	29	427.896	20.973	0.894	36	427.896

NOTE—Column 1 and 2 are equatorial coordinates, Column 3-6 are the median RV, standard deviation, number of exposures and the time baseline in the blue arm, respectively, and Column 7-10 are for the red arm.

APPENDIX

⁵ http://dr7.lamost.org/v1.2/doc/dr7_update

⁶ http://dr7.lamost.org/v1.3/doc/dr7_update

A. CROSS-CORRELATION FUNCTION (CCF)

In this section, we explain our definitions of mean, variance, covariance, and CCF. Let \mathbf{X} denote a vector containing N elements $\{X_i\}$ (e.g., a continuum-normalized spectrum with N pixels), the mean is defined as

$$\bar{\mathbf{X}} = \frac{1}{N} \sum_i X_i, \quad (\text{A1})$$

and the variance as

$$\text{Var}(\mathbf{X}) = \frac{1}{N} \sum_i (X_i - \bar{\mathbf{X}})^2, \quad (\text{A2})$$

and the covariance of two vectors \mathbf{X} and \mathbf{Y} as

$$\text{Cov}(\mathbf{X}, \mathbf{Y}) = \frac{1}{N} \sum_i (X_i - \bar{\mathbf{X}})(Y_i - \bar{\mathbf{Y}}). \quad (\text{A3})$$

A normalized cross-correlation function can be calculated with standardized f and g , namely

$$\text{CCF}(v|\mathbf{F}, \mathbf{G}) = \frac{\text{Cov}(\mathbf{F}, \mathbf{G}(v))}{\sqrt{\text{Var}(\mathbf{F})\text{Var}(\mathbf{G}(v))}}, \quad (\text{A4})$$

where \mathbf{F} is one vector and $\mathbf{G}(v)$ is the other vector but shifted by radial velocity v . When utilizing this CCF to estimate stellar RVs, the $\mathbf{G}(v)$ is usually a spectral template whose signal-to-noise ratio is infinite and covers the wavelength range of \mathbf{F} . Therefore, the shift could be implemented with an interpolation. The CCF in this form is essentially the linear correlation coefficient and varies between -1 and 1 .

B. BIAS IN SMALL NUMBER STATISTICS

The estimators that characterize dispersion are often underestimated when the number of samples is small. For example, if we only have 3 or 5 measurements of a physical quantity, the standard deviation could be underestimated. In this section, we propose an empirical correction of this bias for the error of mean and standard deviation assuming Gaussian distribution $P(x|\mu, \sigma)$ where μ is its position and σ is its standard error.

B.1. The Deviation of Mean

We can minimize an L_1 -norm or L_2 -norm cost function, namely, $\sum_i |x_i - \hat{\mu}|$ and $\sum_i (x_i - \hat{\mu})^2/2$, respectively, to get an estimate of the mean $\hat{\mu}$. The true deviation is by definition

$$\delta_{\text{true}} = |\hat{\mu} - \mu|. \quad (\text{B5})$$

However, in practice we do not know μ when we tackle such a problem. A fiducial deviation associated with $\hat{\mu}$

C. SEVERAL RELATED PYTHON PACKAGES

Three packages are developed in this work.

can be constructed using the 84 and 16 percentiles (or interquantiles, see [Lupton 1993](#); [Ivezić et al. 2014](#)), i.e.,

$$\delta_{\text{est}} = \frac{\{x_i\}_{q84} - \{x_i\}_{q16}}{2\sqrt{N}}, \quad (\text{B6})$$

where N is the sample size. To obtain an empirical relation between δ_{est} and δ_{true} , we assume the following form,

$$\delta_{\text{true}} = \delta_{\text{est}}/\xi(N), \quad (\text{B7})$$

where the $\xi(N)$ is the empirical correction factor and is a function of N . Then, we draw mock data from a standard Gaussian distribution with the `numpy.random` module. In each experiment, we draw N samples and calculated δ_{est} and δ_{true} , and derive ξ . We repeat this experiment for 3000 times for each N ranges from 2 to 250 which is enough for our purpose, and show the 16, 50 and 84th percentiles of the results for each N in the left panel of [Figure 15](#). It is obvious that this fiducial deviation is underestimation of δ_{true} . The relation between medians of $\log \xi$ and $\log N$ is fitted with a 5th order polynomial function, whose coefficients are tabulated in [Table B.1](#). With this relation, we can scale the fiducial deviation to a standard that is less affected by the sample size N .

B.2. The Standard Error

For a Gaussian distribution $P(x|\mu, \sigma)$, we can use sample-based standard deviation and the 16 and 84th percentiles to estimate the true standard error σ , i.e.,

$$\sigma_{\text{est}} = \sqrt{\frac{\sum_i (x_i - \hat{\mu})^2}{N - 1}}, \quad (\text{B8})$$

and

$$\sigma_{\text{est}} = \frac{\{x_i\}_{q84} - \{x_i\}_{q16}}{2}, \quad (\text{B9})$$

respectively. We define ζ by

$$\sigma_{\text{true}} = \sigma_{\text{est}}/\zeta(N), \quad (\text{B10})$$

The results clearly show that both method underestimate the standard error. Similar to the procedures in the previous test, we fit the relation with a 5th order polynomial to the medians of ζ and $\log_{10} N$, the best-fit polynomials are shown in the right panel of [Figure 15](#) and coefficients are tabulated in [Table B.2](#). Compared to [Eq. \(B8\)](#), [Eq. \(B9\)](#) is more robust to outliers but suffers from more significant underestimation when N is small.

1. `laspec` ([Zhang 2020a](#)): A toolkit for LAMOST MRS/LRS spectra, including modules for file IO,

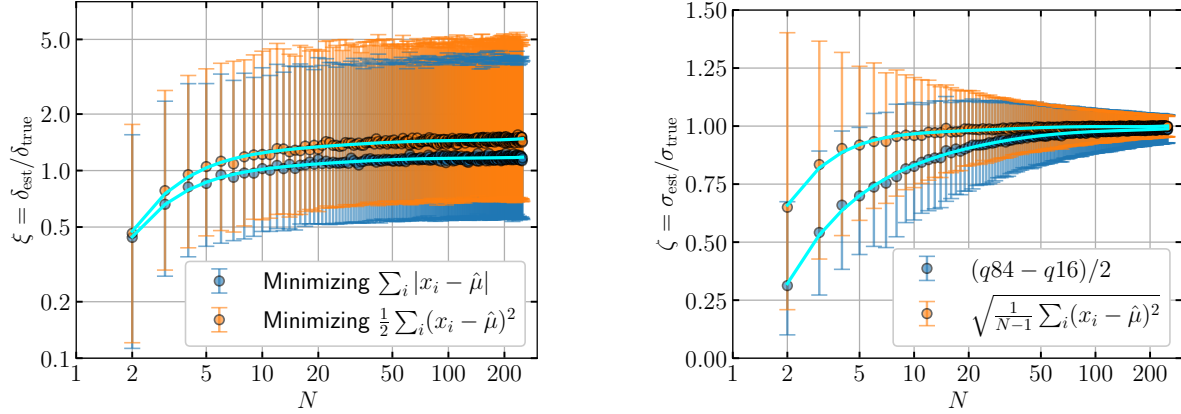


Figure 15. The empirical correction factor for error of mean (ξ) and for standard error (ζ) of Gaussian distributions in small number statistics.

Table B.1. The best fit coefficients of the 5th order polynomials for the empirical relationship between $\log_{10} \xi$ and $\log_{10} N$.

Cost function	β_5	β_4	β_3	β_2	β_1	β_0
$\sum_i x_i - \hat{\mu} $	0.07349721	-0.60647022	1.97806105	-3.22994084	2.72007585	-0.92812989
$\sum_i (x_i - \hat{\mu})^2 / 2$	0.08434813	-0.69694429	2.28047526	-3.73821453	3.15612997	-0.99158461

NOTE—Our definition of polynomial is $\text{Poly}(x|\beta) = \sum_i \beta_i x^i$.

Table B.2. The best-fit coefficients of the 5th order polynomials for the empirical relationship between ζ and $\log_{10} N$.

Estimator	β_5	β_4	β_3	β_2	β_1	β_0
$(q84 - q16)/2$	0.05712779	-0.47050592	1.56888875	-2.75649024	2.71900493	-0.28637106
$\sqrt{\frac{1}{N-1} \sum (x_i - \hat{\mu})^2}$	0.08344418	-0.68630504	2.21084202	-3.50529186	2.77854093	0.08576048

- spectral convolution, continuum normalization, removal of cosmic rays, cross-correlation function and the empirical correction evaluation (Appendix B).
- regli (Zhang 2020b): REgular Grid Linear Interpolator, a multi-dimensional linear interpolator based on gridded data. It is faster than the `scipy.interpolate.LinearNDInterpolator` in the python standard library in our performance test.

- berliner (Zhang 2020c): A toolkit for manipulating the MIST (Dotter 2016) and PARSEC (Bresnan et al. 2012) stellar evolutionary tracks and isochrones, including a python interface to download PARSEC isochrones from the CMD 3.4 website <http://stev.oapd.inaf.it/cgi-bin/cmd>.

The source code and some tutorials of these packages can be found at <https://github.com/hypergravity>. Readers who are interested in LAMOST MRS spectra might find them useful for their research.

REFERENCES

- Allende Prieto, C., Koesterke, L., Hubeny, I., et al. 2018, A&A, 618, A25, doi: [10.1051/0004-6361/201732484](https://doi.org/10.1051/0004-6361/201732484)
- Astropy Collaboration, Price-Whelan, A. M., Sipőcz, B. M., et al. 2018, AJ, 156, 123, doi: [10.3847/1538-3881/aabc4f](https://doi.org/10.3847/1538-3881/aabc4f)

- Bird, S. A., Xue, X.-X., Liu, C., et al. 2020, arXiv e-prints, arXiv:2005.05980. <https://arxiv.org/abs/2005.05980>
- Bressan, A., Marigo, P., Girardi, L., et al. 2012, MNRAS, 427, 127, doi: [10.1111/j.1365-2966.2012.21948.x](https://doi.org/10.1111/j.1365-2966.2012.21948.x)
- Buder, S., Sharma, S., Kos, J., et al. 2020, arXiv e-prints, arXiv:2011.02505. <https://arxiv.org/abs/2011.02505>
- Castelli, F., & Kurucz, R. L. 2003, in *Modelling of Stellar Atmospheres*, ed. N. Piskunov, W. W. Weiss, & D. F. Gray, Vol. 210, A20. <https://arxiv.org/abs/astro-ph/0405087>
- Cropper, M., Katz, D., Sartoretti, P., et al. 2018, A&A, 616, A5, doi: [10.1051/0004-6361/201832763](https://doi.org/10.1051/0004-6361/201832763)
- Cui, X.-Q., Zhao, Y.-H., Chu, Y.-Q., et al. 2012, *Research in Astronomy and Astrophysics*, 12, 1197, doi: [10.1088/1674-4527/12/9/003](https://doi.org/10.1088/1674-4527/12/9/003)
- De Silva, G. M., Freeman, K. C., Bland-Hawthorn, J., et al. 2015, MNRAS, 449, 2604, doi: [10.1093/mnras/stv327](https://doi.org/10.1093/mnras/stv327)
- Deng, L.-C., Newberg, H. J., Liu, C., et al. 2012, *Research in Astronomy and Astrophysics*, 12, 735, doi: [10.1088/1674-4527/12/7/003](https://doi.org/10.1088/1674-4527/12/7/003)
- Dotter, A. 2016, ApJS, 222, 8, doi: [10.3847/0067-0049/222/1/8](https://doi.org/10.3847/0067-0049/222/1/8)
- El-Badry, K., Ting, Y.-S., Rix, H.-W., et al. 2018, MNRAS, 476, 528, doi: [10.1093/mnras/sty240](https://doi.org/10.1093/mnras/sty240)
- Fu, J.-N., Cat, P. D., Zong, W., et al. 2020, *Research in Astronomy and Astrophysics*, 20, 167, doi: [10.1088/1674-4527/20/10/167](https://doi.org/10.1088/1674-4527/20/10/167)
- Gaia Collaboration, Prusti, T., de Bruijne, J. H. J., et al. 2016, A&A, 595, A1, doi: [10.1051/0004-6361/201629272](https://doi.org/10.1051/0004-6361/201629272)
- Gaia Collaboration, Brown, A. G. A., Vallenari, A., et al. 2018, A&A, 616, A1, doi: [10.1051/0004-6361/201833051](https://doi.org/10.1051/0004-6361/201833051)
- Gao, S., Liu, C., Zhang, X., et al. 2014, ApJL, 788, L37, doi: [10.1088/2041-8205/788/2/L37](https://doi.org/10.1088/2041-8205/788/2/L37)
- Gao, S., Zhao, H., Yang, H., & Gao, R. 2017, MNRAS, 469, L68, doi: [10.1093/mnras/rlx048](https://doi.org/10.1093/mnras/rlx048)
- Gilmore, G., Randich, S., Asplund, M., et al. 2012, *The Messenger*, 147, 25
- Gu, W.-M., Mu, H.-J., Fu, J.-B., et al. 2019, ApJL, 872, L20, doi: [10.3847/2041-8213/ab04f0](https://doi.org/10.3847/2041-8213/ab04f0)
- Huang, Y., Liu, X. W., Chen, B. Q., et al. 2018, AJ, 156, 90, doi: [10.3847/1538-3881/aacda5](https://doi.org/10.3847/1538-3881/aacda5)
- Ivezić, Ž., Connelly, A. J., VanderPlas, J. T., & Gray, A. 2014, *Statistics, Data Mining, and Machine Learning in Astronomy*
- Jönsson, H., Holtzman, J. A., Allende Prieto, C., et al. 2020, AJ, 160, 120, doi: [10.3847/1538-3881/aba592](https://doi.org/10.3847/1538-3881/aba592)
- Katz, D., Munari, U., Cropper, M., et al. 2004, MNRAS, 354, 1223, doi: [10.1111/j.1365-2966.2004.08282.x](https://doi.org/10.1111/j.1365-2966.2004.08282.x)
- Katz, D., Sartoretti, P., Cropper, M., et al. 2019, A&A, 622, A205, doi: [10.1051/0004-6361/201833273](https://doi.org/10.1051/0004-6361/201833273)
- Kurucz, R. L. 1979, ApJS, 40, 1, doi: [10.1086/190589](https://doi.org/10.1086/190589)
- Liu, C. 2019, MNRAS, 490, 550, doi: [10.1093/mnras/stz2274](https://doi.org/10.1093/mnras/stz2274)
- Liu, C., Fu, J., Shi, J., et al. 2020, arXiv e-prints, arXiv:2005.07210. <https://arxiv.org/abs/2005.07210>
- Liu, J., Zhang, H., Howard, A. W., et al. 2019a, *Nature*, 575, 618, doi: [10.1038/s41586-019-1766-2](https://doi.org/10.1038/s41586-019-1766-2)
- Liu, N., Fu, J.-N., Zong, W., et al. 2019b, *Research in Astronomy and Astrophysics*, 19, 075, doi: [10.1088/1674-4527/19/5/75](https://doi.org/10.1088/1674-4527/19/5/75)
- Luo, A. L., Zhao, Y.-H., Zhao, G., et al. 2015, *Research in Astronomy and Astrophysics*, 15, 1095, doi: [10.1088/1674-4527/15/8/002](https://doi.org/10.1088/1674-4527/15/8/002)
- Lupton, R. 1993, *Statistics in theory and practice*
- Majewski, S. R., Schiavon, R. P., Frinchaboy, P. M., et al. 2017, AJ, 154, 94, doi: [10.3847/1538-3881/aa784d](https://doi.org/10.3847/1538-3881/aa784d)
- Mészáros, S., Allende Prieto, C., Edvardsson, B., et al. 2012, AJ, 144, 120, doi: [10.1088/0004-6256/144/4/120](https://doi.org/10.1088/0004-6256/144/4/120)
- Morton, D. C. 2000, ApJS, 130, 403, doi: [10.1086/317349](https://doi.org/10.1086/317349)
- Moultaka, J., Ilovaisky, S. A., Prugniel, P., & Soubiran, C. 2004, PASP, 116, 693, doi: [10.1086/422177](https://doi.org/10.1086/422177)
- Nelder, J., & Mead, R. 1965, *Comput. J.*, 7, 308
- Nidever, D. L., Holtzman, J. A., Allende Prieto, C., et al. 2015, AJ, 150, 173, doi: [10.1088/0004-6256/150/6/173](https://doi.org/10.1088/0004-6256/150/6/173)
- Pedregosa, F., Varoquaux, G., Gramfort, A., et al. 2012, arXiv e-prints, arXiv:1201.0490. <https://arxiv.org/abs/1201.0490>
- Press, W. H., Teukolsky, S. A., Vetterling, W. T., & Flannery, B. P. 2002, *Numerical recipes in C++ : the art of scientific computing*
- Ren, J.-J., Wu, H., Wu, C.-J., et al. 2020, arXiv e-prints, arXiv:2008.06236. <https://arxiv.org/abs/2008.06236>
- Steinmetz, M., Zwitter, T., Siebert, A., et al. 2006, AJ, 132, 1645, doi: [10.1086/506564](https://doi.org/10.1086/506564)
- Steinmetz, M., Guiglion, G., McMillan, P. J., et al. 2020a, AJ, 160, 83, doi: [10.3847/1538-3881/ab9ab8](https://doi.org/10.3847/1538-3881/ab9ab8)
- Steinmetz, M., Matijević, G., Enke, H., et al. 2020b, AJ, 160, 82, doi: [10.3847/1538-3881/ab9ab9](https://doi.org/10.3847/1538-3881/ab9ab9)
- Tian, H., Liu, C., Wang, Y., et al. 2020, ApJ, 899, 110, doi: [10.3847/1538-4357/aba1ec](https://doi.org/10.3847/1538-4357/aba1ec)
- Tonry, J., & Davis, M. 1979, AJ, 84, 1511, doi: [10.1086/112569](https://doi.org/10.1086/112569)
- Wang, R., Luo, A. L., Chen, J. J., et al. 2019, ApJS, 244, 27, doi: [10.3847/1538-4365/ab3cc0](https://doi.org/10.3847/1538-4365/ab3cc0)
- Wang, S., Qin, H., & Ye, Z. 2010, *Experimental Astronomy*, 28, 195, doi: [10.1007/s10686-010-9198-x](https://doi.org/10.1007/s10686-010-9198-x)
- Wu, C.-J., Wu, H., Zhang, W., et al. 2020, arXiv e-prints, arXiv:2007.05240. <https://arxiv.org/abs/2007.05240>
- Xu, Y., Liu, C., Tian, H., et al. 2020, ApJ, 905, 6, doi: [10.3847/1538-4357/abc2cb](https://doi.org/10.3847/1538-4357/abc2cb)

- Yang, C., Xue, X.-X., Li, J., et al. 2019, *ApJ*, 886, 154, doi: [10.3847/1538-4357/ab48e2](https://doi.org/10.3847/1538-4357/ab48e2)
- Yang, F., Long, R. J., Shan, S.-S., et al. 2020, *ApJS*, 249, 31, doi: [10.3847/1538-4365/ab9b77](https://doi.org/10.3847/1538-4365/ab9b77)
- Yanny, B., Rockosi, C., Newberg, H. J., et al. 2009, *AJ*, 137, 4377, doi: [10.1088/0004-6256/137/5/4377](https://doi.org/10.1088/0004-6256/137/5/4377)
- Zhang, B. 2020a, hypergravity/laspec: A toolkit for LAMOST spectra., Zenodo, doi: [10.5281/ZENODO.4381155](https://doi.org/10.5281/ZENODO.4381155)
- . 2020b, hypergravity/regli: REgular Grid Linear Interpolator, Zenodo, doi: [10.5281/ZENODO.4381160](https://doi.org/10.5281/ZENODO.4381160)
- . 2020c, hypergravity/berliner: A toolkit for stellar tracks and isochrones., Zenodo, doi: [10.5281/ZENODO.4381163](https://doi.org/10.5281/ZENODO.4381163)
- Zhang, B., Liu, C., & Deng, L.-C. 2020a, *ApJS*, 246, 9, doi: [10.3847/1538-4365/ab55ef](https://doi.org/10.3847/1538-4365/ab55ef)
- Zhang, B., Liu, C., Li, C.-Q., et al. 2020b, *Research in Astronomy and Astrophysics*, 20, 051, doi: [10.1088/1674-4527/20/4/51](https://doi.org/10.1088/1674-4527/20/4/51)
- Zhao, G., Zhao, Y.-H., Chu, Y.-Q., Jing, Y.-P., & Deng, L.-C. 2012, *Research in Astronomy and Astrophysics*, 12, 723, doi: [10.1088/1674-4527/12/7/002](https://doi.org/10.1088/1674-4527/12/7/002)
- Zong, W., Fu, J.-N., De Cat, P., et al. 2020, *ApJS*, 251, 15, doi: [10.3847/1538-4365/abbb2d](https://doi.org/10.3847/1538-4365/abbb2d)